University of Modena and Reggio Emilia

Department of engineering "Enzo Ferrari"

Doctorate School in
Information and Communication Technologies
XXXII Cycle

PhD dissertation

Hollow-Core Inhibited Coupling Fibers for biosensing

Tutor:
Prof. Luca Vincetti

Author:
Fabio Giovanardi

Abstract

During the last decades, biosensors have gained more and more interest in several fields due to their particular features in the biochemical analysis. Involved sectors ranging from biomedical area to agri-food industry passing through defense and security. In the literature, several types of biosensors have been studied based on different physical principles such as electrochemical, optical and mechanical (sensitive to mass changes). One of the main features that the market requires is the "label-free" biosensing: the analysis is performed without any analytes alteration. The work described in this dissertation is focused on the conception and development of a new type of fiber-based platform which could be useful and effective for optical biosensing: Hollow core inhibited coupling fibers (HC-ICFs). They are characterized by a microstructured cladding composed of tubes that surround a hollow core. The holes running along HC-ICFs allow the infiltration of biological substances and for biological layers to attach to the air-dielectric interfaces. Compared to other holey fibers, the presence of a hollow core can further increase the infiltration feasibility and sensor sensitivity. Moreover, in HC-ICFs the particular waveguiding mechanism, based on inhibition coupling, makes their transmission properties particularly sensitive to the thickness of the glass structure which composes the microstructured cladding. Thank that, if the molecular interactions between the surface of the glass structure and the target to be detected result into the generation of an additional layer that modifies the thickness of the structure. The target can easily detect by measuring the fiber transmission spectrum. The technique does not require any additional transducer components such as Bragg gratings, amplifying techniques such as nanoparticles, nor coherent sources. The principle is validated with experimental results showing the detection of both proteins as streptavidin and nucleic acid as DNA of genetically modified soybean.

Sintesi

Negli ultimi decenni, i biosensori hanno suscitato un crescente interesse in diversi settori grazie alle loro particolari caratteristiche biochimiche e la numerosità dei settori potenzialmente coinvolti, che spaziano dal biomedicale all'industria agroalimentare, dalla difesa, alla sicurezza. In letteratura scientifica sono stati studiati svariati tipi di biosensori basati su diversi principi fisici come elettrochimici, ottici e meccanici (sensibili a cambiamenti di massa). Una delle caratteristiche principali richieste dal mercato è che il sensore sia "label-free", ovvero che l'analisi venga eseguita senza alcuna alterazione degli analiti. Il lavoro descritto in questa tesi è incentrato sulla dimostrazione teorica e lo sviluppo pratico di un nuovo tipo di piattaforma basata su fibra ideata per il biosensing ottico. Le fibre a nucleo cavo ad accoppiamento inibito (HC-ICF) sono caratterizzate da un rivestimento microstrutturato composto da tubi che circondano un nucleo cavo. I fori che le caratterizzano consentono l'infiltrazione di sostanze biologiche e l'adesione alle interfacce aria-dielettrico di strati biologici. Rispetto ad altre fibre cave aumenta ulteriormente la facilità d'infiltrazione e la sensibilità del sensore. Inoltre, negli HC-ICF il particolare meccanismo di guida d'onda, basato sull'accoppiamento inibito, rende le loro proprietà di trasmissione particolarmente sensibili allo spessore di tubi di vetro che compongono il rivestimento microstrutturato. Grazie a ciò, se le interazioni molecolari tra la superficie della struttura di vetro e la molecola da rilevare creano uno strato aggiuntivo che incrementa lo spessore della struttura, è possibile rilevare la molecola misurando lo spettro di trasmissione delle fibre. La tecnica non richiede alcun componente aggiuntivo come reticoli di Bragg, tecniche di amplificazione come nanoparticelle o sorgenti coerenti. Il principio è validato con risultati sperimentali che mostrano la rilevazione di proteine come la streptavidina e il DNA della soia transgenica.

Contents

List of Figures

List of Tables

A Elisa e Gabriele

Ringraziamenti

Il lavoro descritto in questa tesi di dottorato è il risultato di un percorso durato tre anni durante ho avuto l'opportunità di imparare ed essere partecipe in ambiti di ricerca internazionale di alto livello come quella riguardante le fibre ottiche a nucleo cavo. Tutto questo però non sarebbe stato possibile senza l'aiuto di molte persone. Innanzitutto, vorrei ringraziane il Prof. Luca Vincetti per avermi dato la possibilità di intraprendere il percorso di dottorato e di fare parte come primo nuovo membro del PhEMLab. Grazie ai suoi suggerimenti e alla sua costante e attiva presenza non posso che confermare la mia più grande gratitudine nei suoi confronti.

Un ringraziamento particolare va a Fetah Benabid che mi ha permesso di condurre un periodo presso un centro di ricerca di fama internazionale a Limoges.

Ringrazio tutti i membri del laboratorio Stefano, Federico e Lorenzo con i quali ho potuto passare dei bei momenti. Ovviamente ringrazio anche tutti i vari dottorandi e i già dottorati: Nicolò, Emilio, Tommaso, Pasquale, Giorgio, Alessandro, Martin, Carlo (spero di averli ricordati tutti).

Non posso che ringraziare mia moglie e i miei genitori che mi hanno sostenuto sia moralmente che economicamente. A mia moglie che prima di essere moglie è il mio riferimento vorrei scusarmi per tutti i problemi che sono sorti durante il dottorato. In ogni caso la vita va avanti e dovremo essere pronti a diventare dei bravi genitori nei confronti di Gabriele che nell'attesa del parto non perde tempo per sfinire la madre.

Chapter 1

Introduction

The market size of biosensors is estimated to reach 33.76 billion dollars by 2026 according to the last report by Grand View Research [1]. Biosensors are devices that combine bioreceptor for detecting an analyte (generally contained in a liquid solution) and a transducer to produce a measurable signal. Main applications are related to the medical field where the interest of miniature diagnostic devices and rapid technological advancements are the keys to market growth. Nevertheless, applications in agricultural, food and environment fields represent other interesting markets. In recent years, the demand for simple, disposable, easy to use and inexpensive devices with fast response times has increased significantly, leading to an increase in sales of these products. In literature, there are different kinds of physical mechanisms to detect biological substances. However, the two most promising are those based on electrochemical and optical transduction. Nowadays, electrochemical biosensors are the most common type, since the experience matured by manufacturers in the integrated circuit technology has allowed the development of low cost and reliable biosensors of this type. However, optical biosensors are expected to have the fastest growth in the next years [1].

Optical sensors are promising for several applications, such as drug discovery, including target identification, ligand fishing, assay development, and quality control [2]. Importantly, optical biosensors have an edge over other analytical technologies since they are more specific, more sensitive, more cost-effective, and smaller in size

[3].

The work of this dissertation shows a new kind of platform based on a hollow-core optical fiber biosensor. The main features of this platform are:

- it is a label-free biosensor, the sensing is performed without alteration of the analyte
- intrinsic proprieties allows having high sensitivity
- the cost of the device is closely related to the optical fiber process technology. No high-cost instrumentation is needed.

Another aspect that should be taken into account is the rising of fiber technology, in particular, the hollow core ones, which are supposed to have great potential for a wide range of applications from the delivering the light in UV region [4] up to the propagation of ultrashort pulses [5, 6], passing through application for telecommunication [7] and industrial processing [8]. Moreover, hollow-core fibers through hollow capillaries can make high interaction between light and gases or liquids.

The platform proposed in this thesis takes advantage of the already consolidated biosensing and optical fiber technology to propose a new kind of optical fiber biosensor based on hollow-core fiber. The work described in this dissertation is structured as follow:

In chapter 2 the state of the art of biosensors with a focus on optical biosensors is reported. In chapter 3 a theoretical background of the waveguiding mechanism of optical fiber is included, to make clear the principle of the sensor proposed. Experimental work with the most significant results is described in chapter 4. Chapter 5 is focused on the development of a new kind of fiber useful for different kinds of technological applications. The final considerations and possible future improvements are shown in chapter 6.

Chapter 2

Biosensors Overview

2.1 Biological Sensors Overview

Nowadays the market and the research laboratories require low-cost and easy to use biosensor able to make the rapid analysis of the biological environments and for health-care fields. Moreover, the specific request is that a new type of biological sensor is label-free. Several groups of researchers in the last decades have proposed several architectures of label-free biosensors. From a general point of view, a biosensor is essentially composed into three-parts related to its function:

- biorecognition element
- transducer
- signal processing

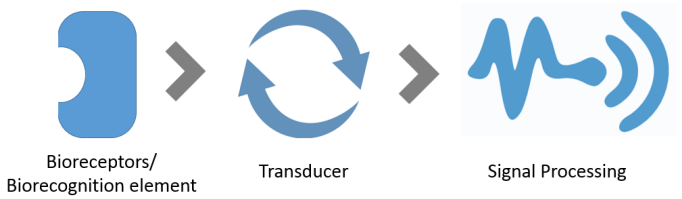

Figure 2.1: Main part of a biosensor: bioreceptor, traducer, signal processing

The aim of biorecognition element, also called bioreceptor, is to provide the analyte specificity for the biosensor. Specificity request a strong and selective affinity between the biorecognition element and target analyte. In particular, the biorecognition element allows the binding of target analytes to produce a signal measurable by the transducer. The transducer is the core of the biosensor; it is the physical platform where the aim is to convert the bio-recognition event (such as the presence of target analyte) into a measurable signal. Then, signal processing (sometimes combined with the transducer part) elaborates on the data to make it available to the user. It consists of a signal conditioning process such as amplification and conversion of signals from analog into the digital form.

Since biosensors are developed by different technological researchers (biologists, engineers, physicists, chemists) can be classified in several ways. In general, a biosensor can be classified in terms of the biorecognition element, biological component or transducer type used.

Based on the biorecognition element it is possible to distinguish: catalytic biosensor, in which interactions result in the formation of a new biochemical reaction product typical of enzyme biosensors and affinity biosensor, in which interactions result in analyte binding onto the transducer surface typical of DNA, and antibodies [9, 10]. Otherwise, the biosensors can be classified according to the biological component used, such as enzymes, antibodies, nucleic acids, or cells. Another classification method that refers to transducer type used. The electrochemical, mechanical/ mass change, optical are the most common, while thermal and magnetic biosensors have less interest.

The potentiometric and amperometric transducers are the most commonly used among all the electrochemical transducers. Amperometric biosensors work at a given potential applied between the working and reference electrodes [11]. A current signal is formed due to the oxidation or the reduction process which is related to the concentration of the analyte [11].

Potentiometric biosensors are based on the potential difference between working and reference electrodes [11]. Its response is proportional to the concentration of the analyte by comparing its activity with the reference electrode [11, 12]. The great advantage of potentiometric biosensors is their sensitivity and selectivity when a highly

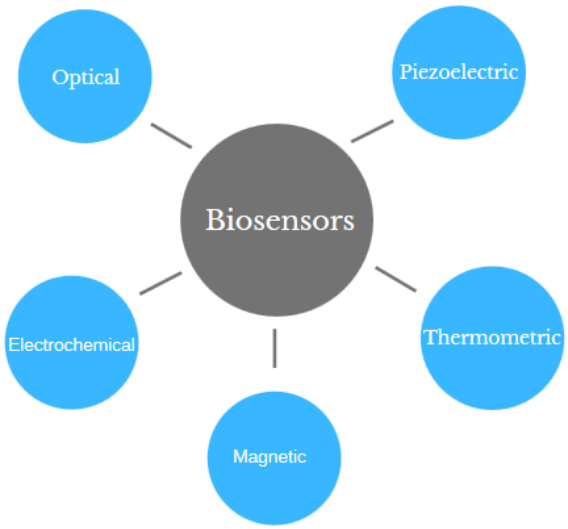

Figure 2.2: Classification of biosensor based on type of traducer

stable and precise reference electrode is used [13].

Since low cost and high reliable electronics technology, electrochemical biosensors are the most used biosensor [12, 14, 15, 16].

Piezoelectric biosensors are of two types: the quartz crystal microbalance and the surface acoustic wave device. They are based on the measurement of changes in the resonance frequency of a piezoelectric crystal due to mass changes in the crystal structure. [17, 18]

As magnetic biosensors are considered miniaturized biosensors detecting magnetic micro- and nanoparticles using the magnetoresistance effect Thermal biosensors or calorimetric biosensors are developed by assimilating biosensor materials into a physical transducer. Magnetic end thermal biosensors in the last years have a low interest by the scientific community probably due to its low reproducibility.

Optical biosensors can be distinguished into two classes, as [19] underlines, based on the detection method. The first one essentially measures light at a fixed wavelength. Absorption and luminescent techniques are the most used because they are simple to use and low cost. However, the main drawback is that they need a stable signal reference. Some techniques as [20] could mitigate this issue. The second one is

based on the detection of wavelength shifts of the transmission or attenuation bands in the spectrum. In general, these configurations are more robust than those based on intensity, since they are independent of the fluctuations of optical intensity. However, they are more expensive, due to monitoring the wavelength shift.

The optical biosensor is a wide category which includes configurations based on photonic crystals ([21, 22]), optical resonators (rings, toroids, cylinders, spheres, ...) [23, 24, 25], integrated optics (planar waveguides, Mach–Zehnder or Michelson interferometers, ...) [26]) and optical fibers.

Regarding optical fiber biosensor, the number of publications over the last years has increased greatly, in particular since 2013 when optical fiber technology is been introduced massively in medicine [19]. This success could be explained by several properties that make optical fibers suitable for different applications [19]:

- **Biocompatibility**: optical fibers are suitable for medical applications due to the material, most of them are made by silica and plastic. Studies [27] [28] have proven that these materials have not side-effect when biological substances interact with them.

- **Reduced size and low weight**: allowing fibers to be inserted into the human body to illuminate inner cavities [29] or to monitor physical variables with a catheter [30]. Therefore, it is feasible to reach places in the human body with light invasive methods avoiding surgery.

- **Low cost**: the success of fiber-optic communications has made it possible to reduce production costs.

- **Ability to work in hazardous environments**: optical fiber has shown good performance working in harsh conditions, as nuclear environment [31] or in the ocean [32].

- **Immunity to electromagnetic fields**: optical fiber sensors, unlike electrochemical sensors, are intrinsically not sensitive to electromagnetic fields.

- **Multiparameter sensing**: multiplexing and integrating signals from different sensors it is possible to monitor several parameters both in the domain of time

and wavelength [33] [34].

- **Different possible configurations of use**: the optical fiber can be used as a cable that guides the light with different configurations such as reflection, transmission.

The present work will focus on novel optical fiber biosensor which is based on wavelength shift, since they are sensitive and reliable in terms of signal to noise ratio.

2.2 Principle of Optical Biosensors

For a general point of view, biosensors except those based on spectroscopic detection (as SERS) have the same basic principle in common: they detect a biolayer. The biolayer is a simplified representation of the chemical bonding created during the detection step. In other words, the biolayer is the result of the immobilization of the target when is bonded with the probe. As will be described in the following paragraphs, only spectroscopy-based biosensors (such as SERS) do not have this detection type.

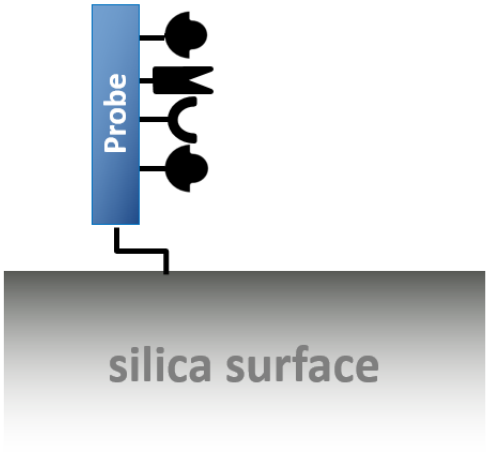

Figure 2.3: Functionalization of silica surface

A crucial feature for biosensing based on biosensor is the selectivity: probe must link only with the right target 2.4. If the target molecule is present, the bonding creates a link on the silica surface increasing its thickness. On the contrary, if the

target does not match the probe the bonding cannot happen, therefore the creation of any layers is not possible. According to these assumptions, the biosensor acts as a lie detector.

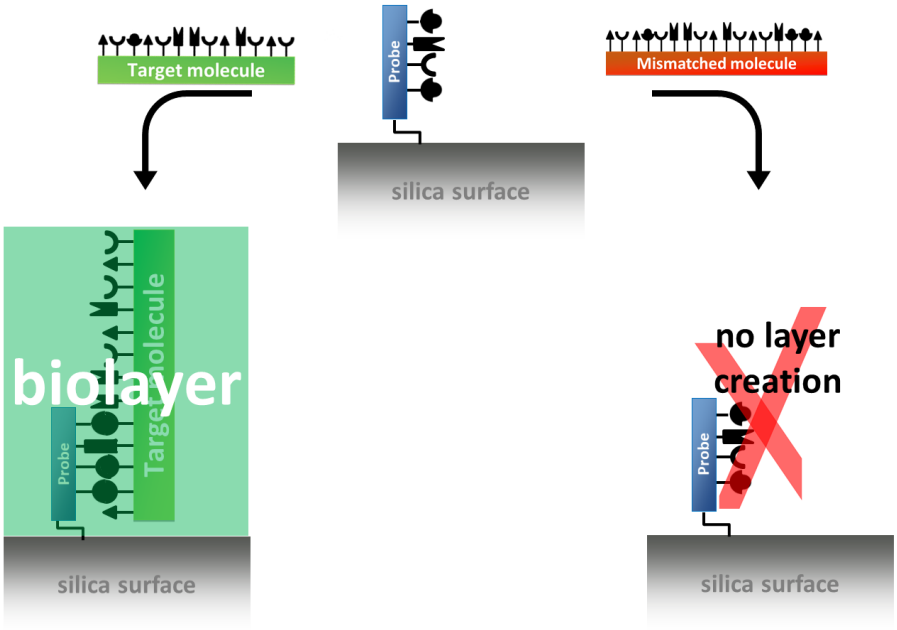

Figure 2.4: Representation of the principle of sensing

From a practical point of view, the biolayer can be described as a homogeneous medium with a refractive index n_{ly} and thickness th_{ly}.

2.3 Fiber Optics Biosensors

Fiber Optics biosensors are considered, as mention above, as optical biosensors. Fiber-optic biosensors (usually abbreviated as FOBS) are device based on optical fiber which use light to measure biological species such as cells, proteins, and DNA. Fiber optic cables have intrinsic properties for which are considered a useful platform for biological sensing. Since their efficiency, accuracy, low cost, FOBS are promising alternatives to traditional immunological methods for biosensing [35].

This dissertation focuses on the differentiating factors of fiber-optic biosensors, which can be categorized as described by Vaiano[36], where the position of the sample

in the fiber represents the key element, or as described by Socorro [19], according to whom the transduction mechanism is discriminating.

2.3.1 Classification of Optical Fiber Biosensor based on the Position of Biolayer

In general, FOBS can be classified into three different categories depending on their structure. In particular, we can distinguish according to where the biological layer (abbreviating biolayer) is deposited: on the tip 2.5a) and over the length, 2.5b), externally or internally.

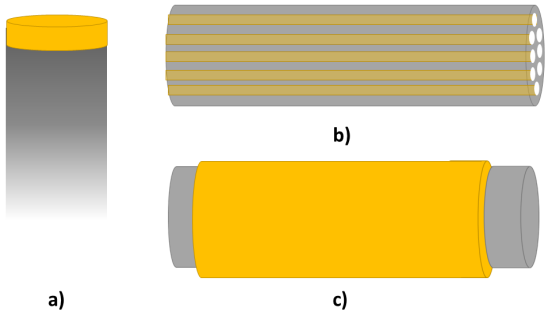

Figure 2.5: Classification of Optical Fiber Biosensors based on the Position of the Biolayer on the Fiber: (a) tip , internally (b) and c) externally

Let's see the main features of these different platforms:

- Biolayer on the tip biosensors: They are kinds of devices based on the measurement of the reflected light that interacts with the biolayer. The tip of the fiber is structured to emphasize interaction. Recently, it is been proved how one particular kind of surface, the metasurface, is useful for biosensing applications[37]. However, these types of structure require several productive steps to obtain a high-quality surface of the tip: this is why this kind of biosensors are not very common [36].

- Biolayer on the length: devices that take advantages form the entire length to detect the biological substances.

  The external type is the most common: it has been the first one to be introduced and it is widely studied and implemented thanks to its simplicity. In

fact, it allows taking advantage of the intrinsic properties of the standard optical fiber. The light is internally confined by the cladding and core medium of the fiber, it follows a path as in 2.6, technically this is known as a total internal reflection (TIR). In this kind of fiber, both the cladding and the core are solid.

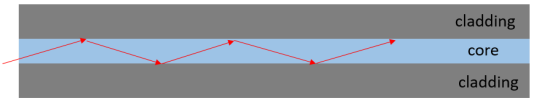

Figure 2.6: Schematic representation of total internal reflection (TIR) in optical fiber

The fibers with this kind of platform are the so-called standard optical fiber or step-index fibers. Thanks to their usage in the telecommunication industry, their cost of production is really low: this has allowed their usage also in the biological field.

About the internal type, the layer is placed inside the fiber, and this guarantees a greater interaction between light and the biological material. Different kinds of photonic crystal fibers with hollow capillaries can be used for this purpose. Commonly, this kind of fibers is also called microstructured fiber. From a general point of view, these fibers can be classified into two main categories: holey cladding fibers, hollow-core fibers as shown in figure 2.7.

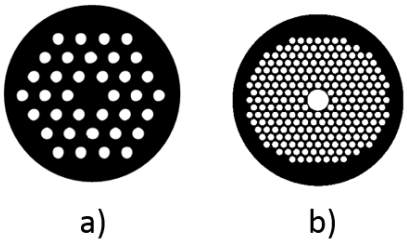

Figure 2.7: Two main typologies of hollow fibers: a) solid-core with holey cladding fiber b) hollow-core fiber

The biosensor proposed in this thesis is based on a hollow-core fiber.

2.3.2 Classification of Optical Fiber Biosensor based on Transduction Mechanism

The classification of the transduction mechanism is the most common one, due to the affinity to the principle of function of the biosensor. Regarding optical fiber biosensors in the literature it is possible to identify five possible mechanisms:

- Evanescent wave fiber optics biosensors
- Biosensors with optical fiber gratings
- Interferometric Fiber-Based Optical Biosensors
- Surface Plasmon resonance (SPR) biosensors
- Surface-enhanced Raman scattering (SERS) biosensors

Evanescent Wave Fiber Optics Biosensors

The sensing mechanism of the external type fiber biosensor is related to the evanescent wave of the mode field of the guide. Considering a single mode fiber for the sake of simplicity, the Gaussian-like profile of the fundamental mode decades with exponential law close to the core-cladding interface and therefore the interaction between the light and the biolayer is extremely low.

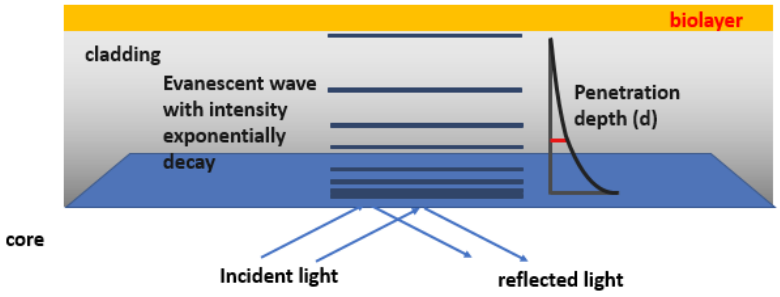

Figure 2.8: Representation of biosensor based on evanescent wave

The penetration depth (d_p) of the evanescent field is a crucial parameter. It is defined as the distance from the interface at which the amplitude of the electric

field is decreased by a 1/e factor [38]. The penetration depth can be expressed as approximated formula [39]:

$$d_p = \frac{\lambda}{2\pi\sqrt{n_{core}^2 sin^2(\theta) - n_{cladding}^2}} \tag{2.1}$$

where n_{core} and $n_{cladding}$ are respectively the core and cladding refractive indices, θ is the incidence angle at the core-cladding interface. The typical penetration depths range is between 100 and 300 nm [40]. Since the penetration depth is really low, several methodologies have been developed to modify the sensing region of standard optical fiber. By changing the cladding structure, it is possible to enhance the light-biolayer interaction increasing the performances of the sensing. For example, by tapering 2.9 c) the fiber [41], [42], it is possible to thin the cladding in sensing area, thus increasing the sensitivity of the sensor. Other cladding modifications remove trough etching methods a portion of the cladding. These fibers are called D-shaped due to their shape after the modification 2.9 b). Often they are used in combination with surface plasmon resonance (SPR) or Localized Surface Plasmon Resonance (LSPR) where the fiber is again modified by a thin layer of metal (as gold or silver) to generate surface plasmon resonance. Compared with SPR, LSPR based sensors are less susceptible to bulk effects: thus, they are more suitable for developing biosensors [43], [44].

Biosensor with Optical Fiber Gratings

Biosensing in biosensor with optical fiber gratings is related to a low change in the phase of the cladding modes. However, this variation is very difficult and high cost to detect using only the fiber and requires the usage of eternal and expensive instrumentation. In order to overcome this issue, usually, an additional component is added to the fiber: its role is to convert the phase variations into amplitude variations, which are very easy to be measured. This component is usually a Bragg grating, a structure formed by several layers of alternating materials characterized by different refractive indices or by periodic variations of some characteristics of the dielectric waveguide. The basic principle of fiber Bragg Grating is a device that reflects a particular wavelength (λ_B) and transmits all other wavelengths. This is obtained by creating a

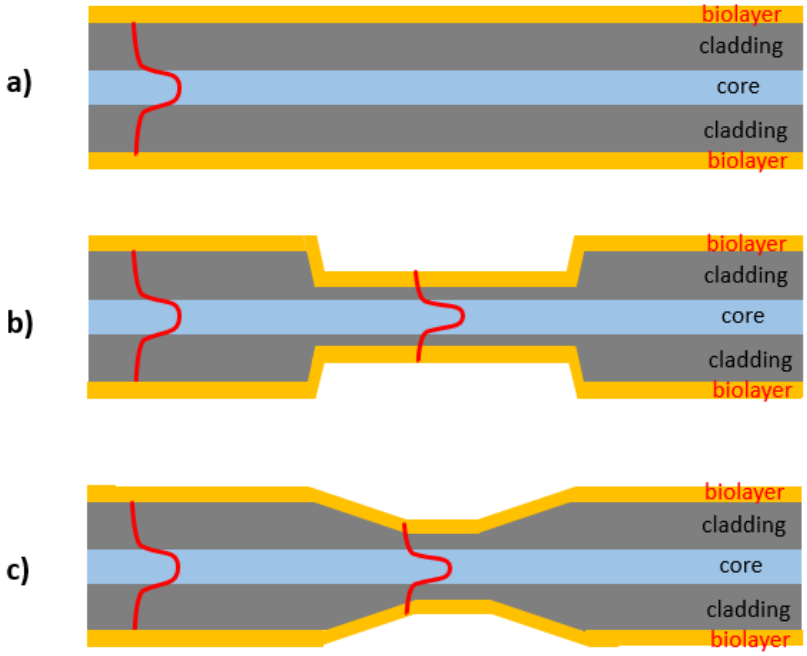

Figure 2.9: Three common optical fiber biosensors with external: a) standard optical fiber b) D-shaped optical fiber c) tapered optical fiber

periodic variation in the refractive index of the core as shown in figure 2.10, which summarizes the principle of function of fiber Bragg grating.

It is possible to make changes changing the periodicity (Λ): short, long fiber Bragg grating (FBGs and LPFGs) and tilted FBGs (TFBGs) are the most common types. Several biosensors configurations with optical fiber gratings can be found in a recent review about fiber Bragg gratings [45]. In particular, the reader can find an interesting deepening about FBGBs based on hollow PCFs with internal biolayer [46, 47, 48] .

Interferometric Fiber-Based Optical Biosensors

From a general point of view, an optical interferometer is a useful device for making precise light measurements. It divides a beam into two or more beams, which travel unequal paths and whose intensities interfere with each other. In other words, an optical interferometer is a phase modulation device based on the overlap of different modes that propagate within an optical waveguide [49] [19]. In order to mathemati-

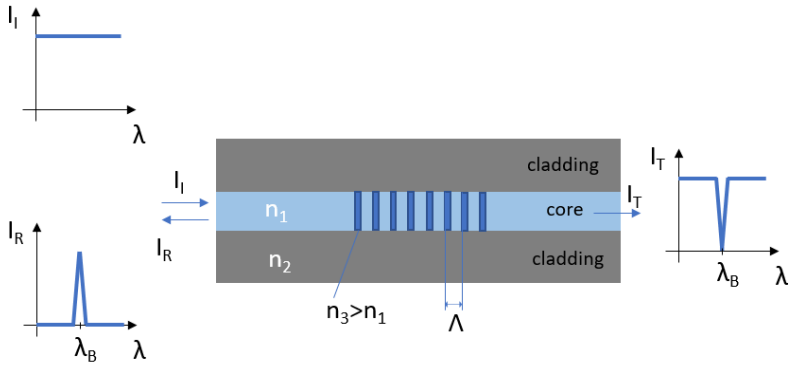

Figure 2.10: Graphical representation of fiber Bragg grating

cally solve the interference of two beams, the general formula is the following one:

$$I = I_1 + I_2 + 2I_1I_2cos(\theta) \tag{2.2}$$

where I_1 and I_2 are the intensities of each beam and $\theta = \theta_1 - \theta_2$ is the phase delay. Interferometric techniques can be used in different fields of application; the two main ones are integrated optical interferometry and fiber interferometry. Sagnac and Mach-Zehnder interferometer are the most common configurations for biosensing. About fiber interferometry, in literature, we find different types of biosensors, which exploit interferometric modulation to sense biological samples [50].

SPR Biosensors

A surface plasmon resonance (SPR) is a resonance that occurs during filling a thin metallic film (typically gold or silver) on a dielectric waveguide. Thanks to intrinsic proprieties, a charge density has its maximum intensity at the metal-dielectric interface and then it decays in both metallic film and dielectric surface [51]. SPR biosensors are extensively used with Kretschmann configuration [52]. Basically, when light falls through a prism on a metal surface, a portion of it is reflected on the metal surface. But at a certain incident angle known as a resonant angle, light is absorbed by the charge density. In optical fibers, the excitation process the principle of functioning is similar to Kretschmann's configuration, but it has some peculiarities. Firstly, it is not possible to control the angle of incidence because of the light guided by the optical

fiber. Secondly, the numerical aperture of the fiber strongly limits the range of angles of incidence which satisfy the generation of SPR. Consequently, the detection of the resonance wavelength shift in the optical spectrum is the basis of detection. Moreover, the cylindrical geometry of the fiber is not suitable to maintain a polarized state [53]. Therefore, it is necessary to use an external polarization maintenance system, leading to an increase in the final cost of the device. SPR fiber biosensors are also used in combination with interferometry techniques to increase its performances [54].

SERS Biosensors

Surface-enhanced Raman scattering (SERS) is a technique that enhances the intensity of the molecule vibration of several orders of magnitude when it is close to nano-roughened metallic surfaces made of silver or gold [55]. There are several types of SERS platforms, both planar and fiber-based. Regarding fiber optical based SERS conventional type fiber has proposed platform on the tip [56, 57]) and over the length with cladding modification techniques (as D-shaped, tapering). Traditionally, SERS fibers fabricated on conventional optical fibers have low sensitivity needed for biosensing. To overcome this limitation, hollow-core photonic crystal fiber has been used to make SERS probes permitting the incorporation of metallic nanoparticles and liquid analytes into air holes [58, 59, 60].

From a general point of view, it is possible to combine the two classifications of biosensors proposed above into a general and summarizing table 2.1. This aim of it, is to make an overview of the flexibility of optical biosensing, combining different layer positions with different mechanisms of transduction. Without any claim of completeness, some references are reported to give to the reader some examples of deepening.

	tip	external	internal
Evanesc. wave	-	[61] [62]	[63]
w Bragg Grating	-	[64]	[65]
w Interferometric	[66]	[67]	[68]
SPR	[69]	[70]	[71]
SERS	[56] [57]	[72]	[73] [58]

Table 2.1: Matrix representation of different type of biosensors based on fiber optics

2.4 Description of the Proposed Platform for Biosensing

The platform of the optical fiber proposed in this thesis is characterized by microstructured cladding and by a hollow core. These characteristics increase the feasibility of the infiltration of liquids and allow high interaction between light and the biological layer. Concerning the table 2.1, the fiber proposed in this thesis belongs to the internal group, but it does not belong to any of the mechanisms-based rows, since it exploits the intrinsic characteristics of the fiber. In fact, it is not needed the usage of Bragg Grating (or interferometric techniques, surface plasmon resonance or other additional components), thanks to its waveguide mechanism shown in section3.2. Therefore, a new line of research in the optical fiber biosensors literature could take a cue from this platform. Basically, the principle of sensing is related to cladding modification: the thickness of the entire structure is increased. The sensing is performed by the detection of a shift of the transmission spectrum.

Summarizing, the biosensor proposed in this dissertation has the following features:

- it is a label-free sensor: the target molecule is detected as it is, any labeled techniques as gold nanoparticles or fluorescence are necessary. - absence of any additional components (as Bragg Grating inscription) or the metallization (any SPRs or SERS techniques are involved) - high sensitivity, due to the proximity of the biolayer to the light

2.5 Label-Based vs. Label-Free Biosensors

Having described two possible classifications proposed by literature from the optical point of view, let's focus on one of the main chemical features in biosensing. The demand for low cost and reliable devices is increased dramatically in the last years. In the biotechnology field the market requests biosensor as a device used for the high number of heterogeneous groups: from the researcher in a chemical laboratory to a small producer of food products such as wine, oil. The offer of the market will satisfy

a huge amount of requests. However, the main tasks are the low price, the reliability and a particular feature that it is called be label-free. The label-free characteristics mean that the recognition of the analyte is not deteriorated at the end of the sensing process. The aim is to leave the analyte intact, free from alterations. The advantages of label-free techniques are faster procedure and the possibility to monitor the bonding in real-time. Moreover, the label is able to interact with the analyte it would interfere during the sensing. From the theoretical point of view, sensing should be simpler due to the absence of labels. On the contrary, label-based detection implies the use of a secondary molecule, the label in order to emphasize the signal or to facilitate the measurement. Colorimetric, fluorescent or luminescent method are the most common methods [74]. One advantage of using labeled detection methods is that the secondary molecule furnishes double check of the detection, limiting the false-positive readings. However, since label-based detection introduces an additional time-consuming step, labeled detection techniques are not proper for fast and real-time sensing applications [75]. The biosensor proposed could be used with both methods. Since the label-free one is the more request, this thesis focuses on it. However, some notes about the label based version are included in the experimental section for the sake of completeness.

Chapter 3

Inhibited Coupling Fibers for Biosensing

This chapter aims to show the theoretical background of the waveguiding mechanisms of optical fibers. After a brief introduction about the different types of waveguiding mechanisms, the inhibited coupling mechanism will be deepened. It will be shown that thanks to intrinsic proprieties, inhibited coupling fiber are suitable for biological detection.

3.1 Overview of Fiber Waveguiding Mechanisms

The waveguiding mechanism plays an important role to understand the proprieties to find new performing applications. It is possible to identify three possible waveguide mechanisms for propagating the light into a fiber: total internal reflection (TIR), photonic bandgap (PBG) and inhibited coupling (IC), also called as antiresonant.

TIR is the most common mechanism since it belongs to the standard fiber: step-index fiber. It is characterized by a solid core surrounded by a solid cladding with a lower refractive index. The small difference between core and cladding refractive index (typically between 0.001 and 0.02) allows confining the light into the core. The name step-index is related to the shape of the refractive index profile. Since the step-index fibers are made by silica (pure glass) they have a low loss due to the

minimum silica attenuation of 0.2dB/km around 1550nm (this band is frequently used in telecommunication applications and it is called C-band). TIR is limited due to the material proprieties (typically silica). The minimum loss of silica TIR is given by the contribution of Rayleigh scattering and the absorption in the infrared region: this result a limited bandwidth (see figure 3.1).

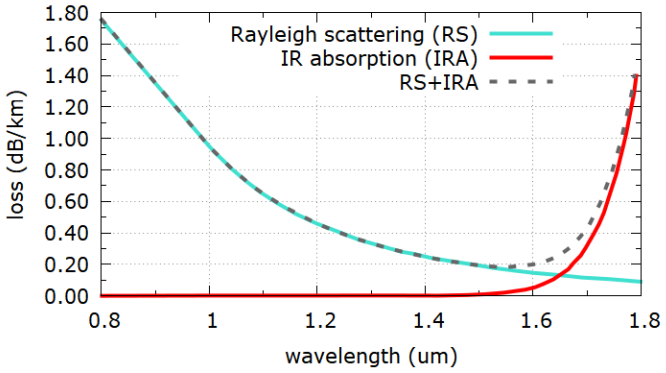

Figure 3.1: Spectral attenuation of silica medium

Other types of fibers are called photonic crystal fiber (PCF) proposed for the first time by Russell in 1995 [76]. It was a disruptive innovation bringing a wider bandwidth and not constrained to a fixed wavelength band. In fact, with this kind of fiber, it is possible to set the spectrum region. The fiber is composed of a microstructured cladding which creates a periodic structure that surrounds a core where the light travels. In PBG fiber the propagation is allowed only where a photonic bandgap of the cladding lattice is present. The study of this fiber is focused on the cross-section because is invariant along the axis direction: considering a periodic lattice as figure 3.2 is it possible to numerically compute the solutions through a finite element simulator. The computation can be simplified considering the elementary cell applying appropriate constraints as which acts as a periodic condition (Floquet-Block theory) [77, 78].

The bandgap can be view as a forbidden region for lattice mode, thus inside the gap, there are not any modes of the structure. Therefore, if a defect is created removing a portion of the lattice, the light inside the bandgap can be guided. In particular, the bandgap is limited by the dispersion curve of the apex (the intersection

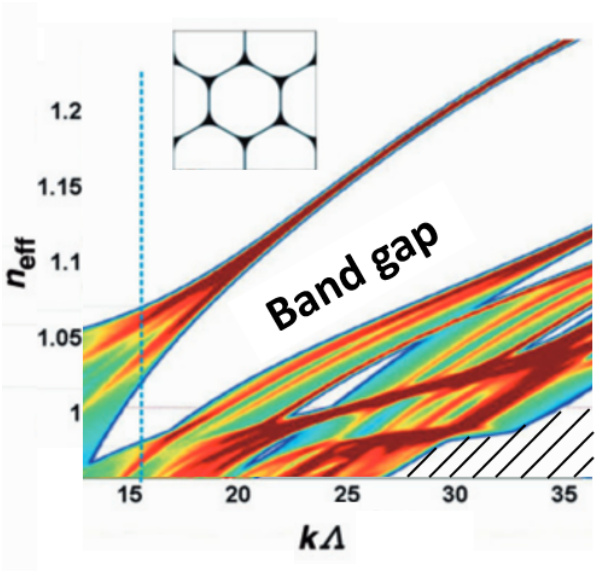

Figure 3.2: State diagram of a periodic triangular lattice. A band gap is present. On the x-axis a normalized axis: k wave-vector, Λ the pitch of the lattice Reprinted with permission from Reference [79], Francis & Taylor, 2011

of lattice), struts and holes modes. Figure 3.3 clarifies this dependence [80] where k is the wavenumber and Λ is the internal size of the cell.

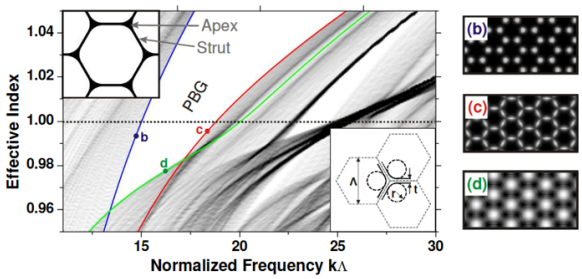

Figure 3.3: Example of photonic band gap in a periodic lattice. In blue, red and green are highlighted the dispersion curve of respectively apes, struts and holes [80]

Compared to TIR, PBG has the advantage related to the possibility to chose the spectral position of the band of transmission. To design the spectral region of operation, it is necessary to correctly design the lattice by choosing to adjust the spectral position of the bandgap. On the contrary, one of the main drawbacks is bandwidth caused by a technological limitation. IC fiber, the last type of mechanism discovered, is based on a theory completely different because it does not have any photonic bandgap. Thanks to intrinsic characteristics ICF overcome limitations on the

bandwidth as PGB fiber. However, this theory is not still complete, there is a debate in the scientific community about some details in the waveguiding mechanism. The main theories of this fibers, both considered valid, are the inhibited coupling mechanism [81] [82] [83] and the antiresonant mechanism [84] [85]. Briefly, the mechanism about the propagation of IC is based on the coupling mode theory. Considering the core mode and cladding mode the propagation is allowed where there is a weak coupling between them [81]. For further details see in section 3.2. While antiresonant fiber is based on the membranes (or cladding layers) which block the leakage reflecting it (as a Bragg grating) [84]. One of the most promising IC fiber types is tube lattice configuration where the dielectric is composed of a tube placed in a circular manner which describes a hollow core. Figure 3.4 summarized fiber waveguiding mechanism.

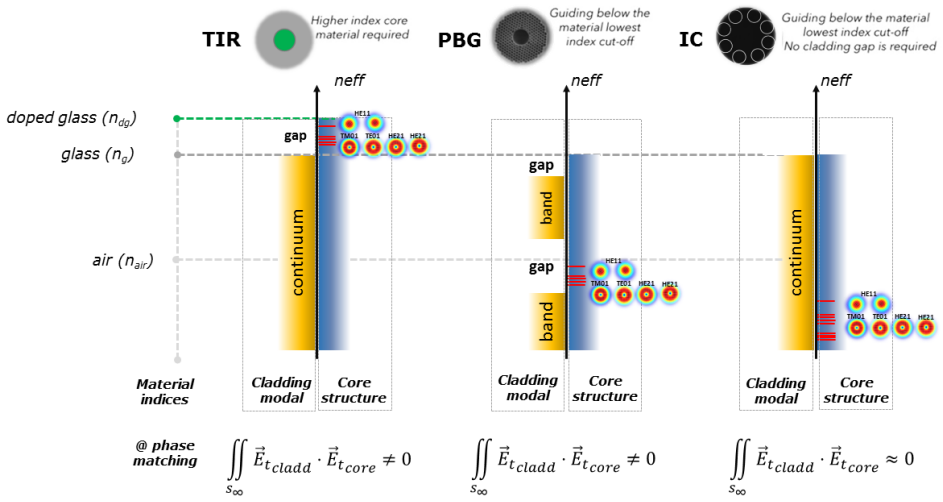

Figure 3.4: Representation of the three waveguide mechanism known: a) TIR, b) PBG, c) IC. This figure is taken by [86]

3.2 Inhibited Coupling Fibers

The most common IC fibers are the kagome lattice fiber, tubular fiber (TLF) and type-cone (or ice-cream) fiber, as figure 3.5 shows.

As already said, in the IC fibers there are not bandgap as the figure 3.6 shows. The mechanism, as the name of the theory suggests, is related to the coupling between core and cladding modes. The details will be explained further (section 3.3).

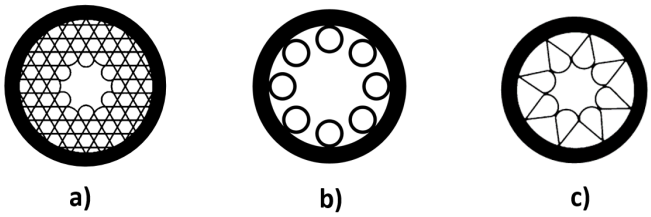

Figure 3.5: The most common ICFs: a) kagome fiber b) tubular fiber c) cone-type fiber

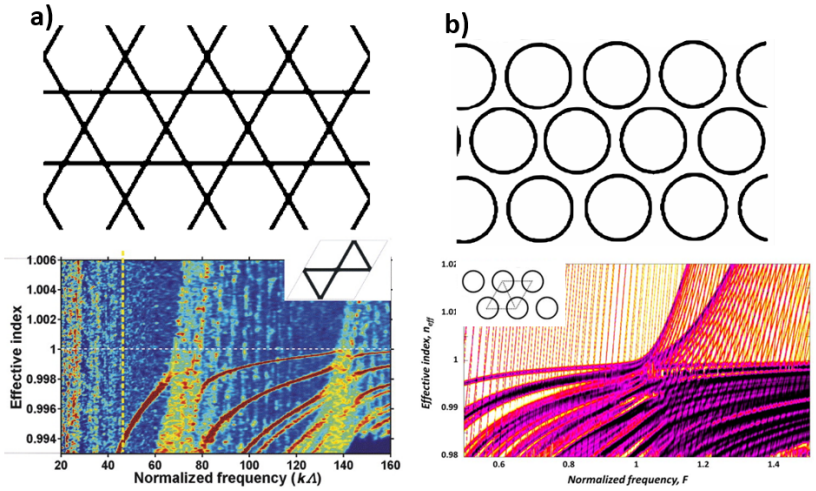

Figure 3.6: Two types of IC lattice: a) kagome lattice [87], b) tube lattice [81]

Figure 3.6 shows a comparison between two different IC lattices: the lattice on the left (a) is a kagome lattice, while the other, on the right it is a circular lattice. Since their diagram is full-colored, they do not have any photonic bandgap. The kagome lattice was used to make the first IC fiber due to its regular shape and its self-support [88]. Its lattice is characterized by a periodic arrangement of a regular hexagon. Technically this arrangement is called periodicity or pitch of the structure and it is denoted by Λ. Fiber with kagome lattice can be distinguished by the number of single elements removed to form the core. The single element is usually called cell. Figure 3.7 shows different typologies of kagome fibers: 1-cell, 7-cells, 19-cells.

On the other side the lattice, figure 3.6 b), is composed of an arrangement of tubes disposed of periodically. As above the periodicity of the lattice is denoted by pitch Λ. Fibers with tubes have simpler geometry than kagome one but their fabrication

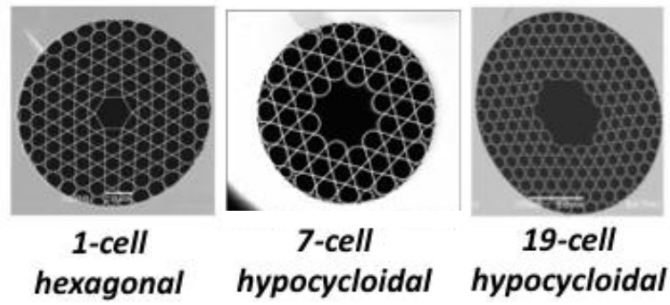

Figure 3.7: SEM images of different types of hollow core kagome fibers: from left to right 1-cell, 7-cells, 19-cells [86]

is more difficult due to few attaching nodes with silica bulk. Thanks to its geometry shape which offers a high number of degree of freedom tubular fiber have a great interest in the scientific community. Figure 3.8 shows three main fiber-based with this type of topology.

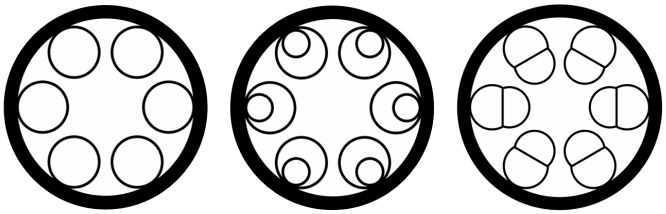

Figure 3.8: Three main typologies based on tubular lattice: from left to right standard TLF [81], nested TLF [84], conjoined TLF [89]

In the last years, novel configurations of inhibited coupling fiber as [89] are promising to reduce the loss contribution which is a fundamental parameter for light propagation.

3.3 Inhibited Coupling Mechanism

In this section, the reader can find essential information to understand the mechanism upon which this fiber delivers light. The waveguiding mechanism is fundamental for the comprehension of the principle of function of biosensor based on inhibited coupling fibers. As previously discussed, inhibited coupling fibers do not have any photonic bandgap thus a new theory is needed to explain this phenomenon. The waveguiding

mechanism of IC fiber can be easily understood displaying in the same diagram of all solutions of the structure. For this aim, it is considered a TLF instead of a kagome for the simplicity of the geometry. The figure 3.9 shows the effective index *neff* of each solution over the normalized frequency. The computation is done by a finite element analysis trough COMSOL Multiphysics through a mode analysis study.

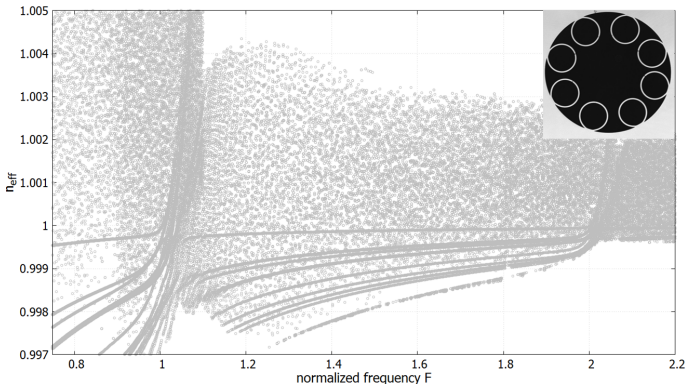

Figure 3.9: Solutions of TLF (expressed as effective index) as a function of the normalized frequency F.

In TLFs the cladding does not exhibit any photonic band-gap as shown in figure 3.9. The cladding modes form a quasi-continuum of solutions without any possibility to form a gap enough bigger to propagate a guided mode. The lattice proposed has plenty of solutions, hence the waveguiding mechanism must be different. Figure 3.10 (a) shows the cross-section of a tube lattice fiber: it is characterized by an hollow core with core diameter D_{co}, which is surrounded by a cladding composed of a regular arrangement of silica tubes with refractive index n_{si}, external diameter D_{ext}, thickness t_{si}, and spaced by δ.

To understand the waveguiding mechanism a mode classification occurs. In a multi-mode optical fiber four different types of mode exist:

- Core Modes: modes where the power is concentrated in the core of the structure, figure 3.10 b)
- Cladding Modes (or dielectric modes): modes where the power is concentrated in the cladding of the structure 3.10 c),d)
- Hole Modes: modes where the power is concentrated in the holes of the structure

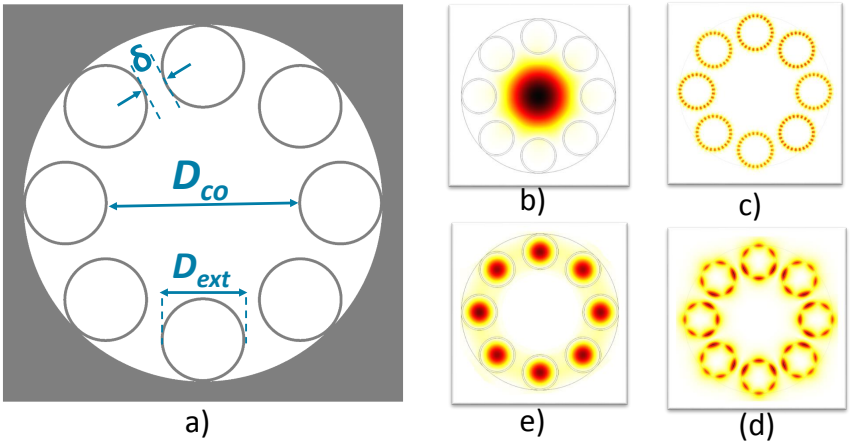

Figure 3.10: (a) Tube Lattice Fiber cross-section; the gray part shows silica, while the and white one air. Field profiles of (b) core mode (c-d) cladding modes with fast and slow spatial dependence, respectively, and (e) hole mode.

3.10 e)

Figures 3.10(b)-(e) show the intensity profile of the fiber modes: core modes, and cladding modes which comprise both silica modes and air hole modes. Core and holes modes are guided modes, hence the mode is well confined and it could propagate along with the guide. On the contrary cladding, modes are leaky (or lossy) and the power delivered by the light is guided outward losing it.

In order to describe the dispersion of the curve of core and holes mode is useful to apply the study of Marcatili and Schmeltzer [90]. They proposed the analytical dispersion of the curve of a structure of an infinitely extended medium that surrounds a hole as shown in figure 3.11 a).

It is an ideal structure, physically unachievable, but useful to understand the modal content. His studies are daily used by hundreds of research all over the world. The formula 3.1 is the following:

$$n_{eff_{nm}} = 1 - \frac{1}{2}\left(\frac{u_{nm}\lambda}{2\pi R}\right)^2 \tag{3.1}$$

where u_{nm} is m^{th} root of n^{th} order Bessel function.

The modes are confined inside the hole and their distribution intensity is $LP_{mn} - like$. Understanding the modal content of studies of Marcatili is useful for the estima-

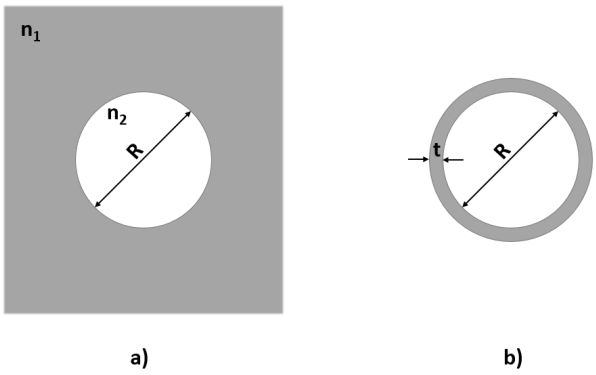

Figure 3.11: a) Structure of Marcatili and Schmeltzer studies. It is a hole with refractive index n_2 surrounded by a different homogeneous n_1, (n_2>n_1), b) tube structure

m	$u_{0,m}$	$u_{1,m}$	$u_{2,m}$	$u_{3,m}$
1	2.048	3.8317	5.1356	6.3802
2	5.5201	7.0156	8.4172	9.7610
3	8.6537	10.1735	11.6198	13.015
4	11.7915	13.3237	14.7960	16.2235

Table 3.1: The fist roots of the Bessel function

tion of the analytical curve of core and hole mode of a tube structure. It is composed of a circular crown with thickness th with refractive index n_{si} which forms a circular air hole with R_{co} radius.

Cladding mode, on the contrary, due to their geometry can not describe as a simple analytical formula. Hence, the cladding mode which can be $HE_{\nu,\mu}$ or $EH_{\nu,\mu}$ needs a detailed study. However, studying the cladding mode of a single tube is useful to understand the waveguiding mechanism of TLF. Figure 3.12 highlights this advantage. In fact, the dispersion curves are coincident: the field distribution of a single tube well describes the distribution of a single tube in a TLF and the entire TLF [91].

For this purpose, it is useful to introduce the normalized frequency F [92]. As the name suggests, is a parameter useful to normalize data and it follows the equation 3.2:

$$F = \frac{2\,t_{si}}{\lambda}\sqrt{n_{si}^2 - n_{air}^2}. \tag{3.2}$$

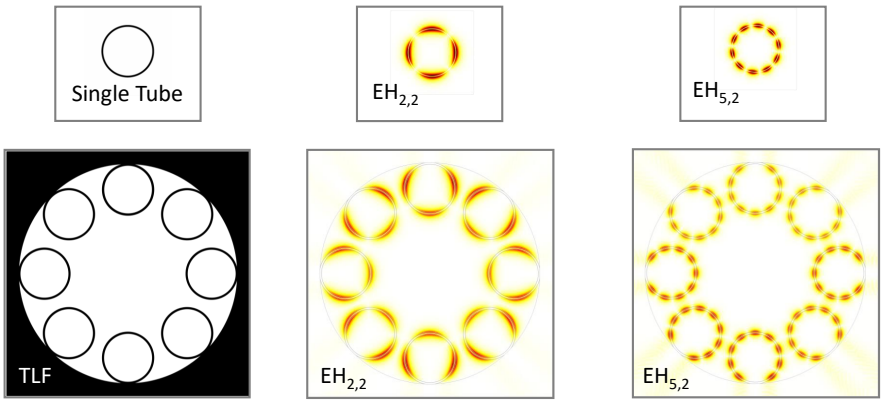

Figure 3.12: Normalized field intensity of $HE_{2,2}$ $HE_{5,2}$ of single tube and TLF

The normalized frequency is introduced to display the wavelength axis regularly; it is useful to avoid spreading or compressing the frequency spectrum. Considering figure 3.13, it can be noticed that the sequence of cladding mode is regular: the position on the spectrum of cladding mode follows a specified order. Considering the cladding mode in the band F= [1;2] is possible to notice, as planned, a progression of μ happens: it starts from low values at F=1 arriving at F=1.5, in the central band $\mu = 22$. Figure 3.13 shows seven EH cladding modes where $\nu = 2$ and μ varying from 2 to 22, the last one begins from $\nu = 3$ and $\mu = 0$.

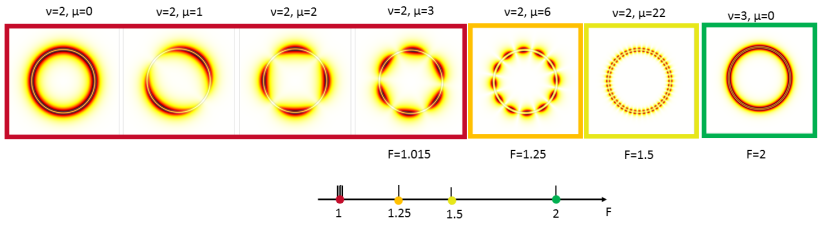

Figure 3.13: Comparison of HE cladding mode varying ν and μ. On the bottom the representation of spectral position in the normalized frequency

At integer values of F, a new type of cladding mode happens with a progressive azimuthal number. It is possible to state that: cladding and hole modes can be described with the Marcatili formula 3.1, while to describe cladding mode is useful to take into account cladding mode of a single tube.

In view of the above, it is possible to introduce the waveguiding mechanism of

inhibited coupling theory which is based on coupled mode theory [82]. According to the couple mode theory two modes are coupled, and thus they exchange power, only when they satisfy two conditions:

- phase matching condition: the phase constant of two modes are the same, therefore also their effective index n_{eff} are equal, in formula:

$$\beta_{mode1} = \beta_{mode2} \tag{3.3}$$

considering that $n_{eff} = \frac{\beta}{k_0}$ and $k_0 = \frac{2\pi}{\lambda}$ where k_0 is the propagation constant

$$n_{eff_{mode1}} = n_{eff_{mode2}} \tag{3.4}$$

- overlap integral of the electric field must different than zero:

$$I = \frac{\pi}{2\lambda} \int_{S_\infty} \overrightarrow{E}_1 \cdot \overrightarrow{E}_2 dS \neq 0 \tag{3.5}$$

The modes that are involved are core modes and cladding modes. For simplicity, it is considered only the fundamental mode as core modes. Figure 3.14 shows the dispersion curve of the core mode and the two dispersion curves of two cladding modes.

Since the fibers work in the large core regime, the effective index of the core mode is very close to 1. While, the distribution of cladding modes is completely different: as a first instance, they are characterized by the different varieties of the oscillations along the azimuthal direction. Considering the intersection points (black points) between core and cladding dispersion curves according to the coupling code theory the phase-matching condition is satisfied: in these points, the phase of two modes is the same, while the overlap integral needs further analysis. It is now possible to compute the overlap integral in the two cases. Between (A) and (B) the overlap integral is different from zero due to slow spatial variation; while (A)-(C) overlap integral is almost zero because the positive and the negative contributions tend to cancel each other. Concluding a strong mode coupling happens only between (A)-(B)

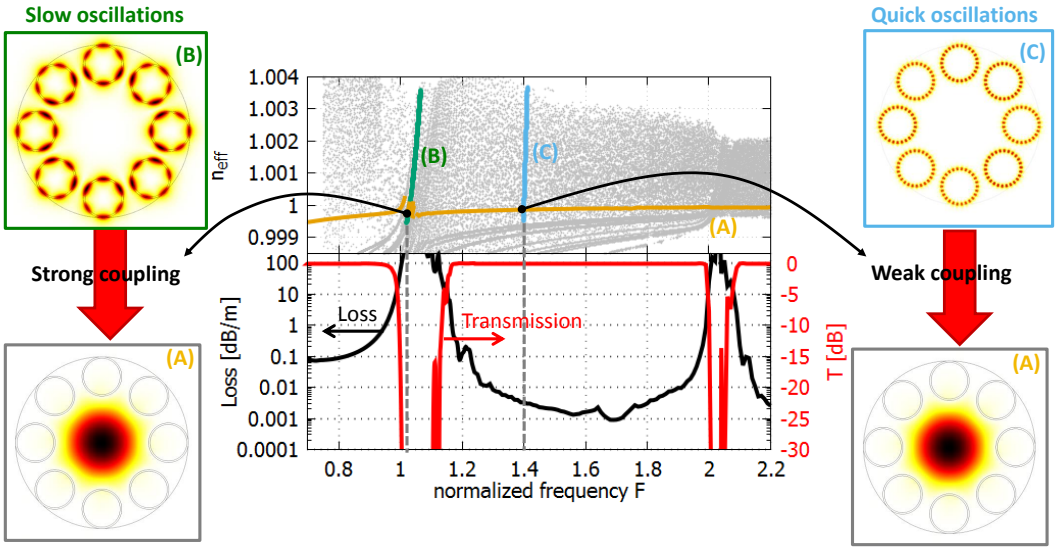

Figure 3.14: IC waveguiding principle. Top: (A), (B), (C) represent the normalized electric field intensity on the fiber cross-section of a core mode, the cladding mode with slow spatial oscillations, and the one with fast spatial oscillations. In the middle there are the dispersion curves (n_{eff} vs F) of the cladding modes (gray zone) and core mode (orange zone); solid lines in green and blue color highlight dispersion curves of the cladding modes (B) and (C) , respectively. In the bottom the black solid line represents the propagation loss of the core mode (A), while a the red line the corresponding transmission spectra of a 30 cm long piece of TLF. Curves show the high loss and low transmission spectral regions due to coupling of the core mode with slowing varying cladding modes, which occur close to the integer values of the normalized frequency F.

where there are satisfied the phase-matching condition and the overlap integral is different from zero. In (A)-(C) case the coupling is very low and for this reason, it is called inhibited. In other words, the coupling leads to high loss (low transmissivity), on the contrary, an inhibited coupling leads to low loss (high transmissivity). This section, it is studied what happens in a portion of the spectrum. Applying this study in a wider spectrum is can be noticed that there is an alternation of high and low transmissivity leading IC fibers to deliver the light in several bands.

In conclusion, in TLFs the transmission spectrum is described by a succession of high and low transmission spectral regions; this spectrum strongly depends on the core mode dispersion curve which crosses with the curves of cladding modes having slow and fast spatial oscillation respectively. Since the dispersion curve of the core

mode is close to the air index $n_{eff} = 1$, the transmission band can be approximated by the cut-off frequencies of the respective slowly varying cladding modes. This can be described by the following formula [82]:

$$F \simeq n, \tag{3.6}$$

In the light of this, the spectral position of the high loss regions can be well estimated by the cut-off wavelength of the $HE_{\nu,1}$ modes of TLF [82]:

$$\lambda_m = \frac{2t_{si}}{m}\sqrt{n_{si}^2 - 1} \tag{3.7}$$

3.4 Concept of the Sensor

The waveguiding mechanism is strictly correlated with the principle of function of the sensor. In fact, thanks to the dependence given by equations (3.6) and (3.2) the spectral positioning of low transmission regions depends on the ratio between tube thickness th_{si} and wavelength. The basic concept of the sensor is the detection of an additional layer laying down on the silica surfaces, as shown in figure 3.15, this layer increases the tube thickness: this increase changes the transmission spectrum which results in a shift toward higher wavelengths. This shift is technically called redshift because the red light has a longer wavelength in the visible spectrum. Supposing the adding thickness is arranged is homogeneous (the thickness is increased by the same amount in each position) the shift is directly proportional to the thickness. The redshift is strictly dependent on the refractive index n_{ly} and thickness t_{ly} of the additional layer. According to ([93]) a biological material has a refractive index around 1.5, very close to the refractive index of the silica medium. Keeping a constant refractive index of the biolayer the spectral shift depends principally on the thickness of the silica plus the thickness of the biological layer.

Since $n_{ly} \approx n_{si}$, according to eqs. 3.2 and 3.7, the thickness of the layer can be estimated as:

$$t_{ly} \approx \frac{\Delta}{2\lambda} t_{si} \tag{3.8}$$

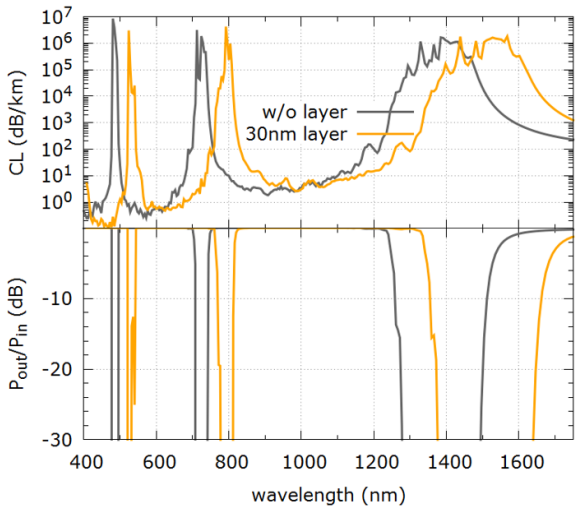

Figure 3.15: TLF cross-section with additional layer of thickness t_{ly} (orange curve) and biolayer : the target molecule binds to the probe, generating the biolayer with refractive index n_{ly}.

being $\delta\Lambda$ the redshift measured by comparing the fiber transmission spectra before and after the biolayer detection. Numerical simulations have been done to demonstrate this peculiar feature of IC-TLF fibers. In order to represent the simulated model as accurate as possible, the cross-section of the fiber (fiber #1) used in the experimental part (4.2) is taken into account ($D_{ext} = 18\mu m$, $t_{si} = 610nm$, $\delta = 4.2\mu m$ and additional layers having different t_{ly} and n_{ly}). Modeling drawn fibers is fundamental to understand the leakage contribution. A study that draws fibers modeling is described in appendix A.1.

Figure 3.15 compares the propagation loss and the transmission spectra of TLF $30\,cm$ long, without and with an additional layer $30\,nm$ thick and with $n_{ly} = 1.5$.

A redshift caused by the additional layer is visible: the spectrum shifts toward higher wavelengths. It is possible to notice that the redshift is greater in higher wavelengths due to its waveguide mechanism (see 3.3). Plotting in normalized frequency F the enlargement and compression of the spectrum is less apparent. The additional layer can be modeled essentially with two parameters: its thickness, which is correlated with the chemical bond, and the refractive index of the biomaterial. In order to demonstrate the feasibility of the concept of the sensor, a deep study has been done changing both parameters. In figure 3.16 the results of the study cover several

possible causes. Figure 3.16 shows the comparison of the transmission spectra of the same TLF. The shown transmission notches correspond to $n = 1$ and $n = 2$ in Eq. (3.6). Even if the biolayer is $5\,nm$ thin and with a low refractive index of 1.1, a redshift of few nanometers can be noticed. Therefore, it can be stated that a very high sensitivity has been got in terms of thickness and refractive index.

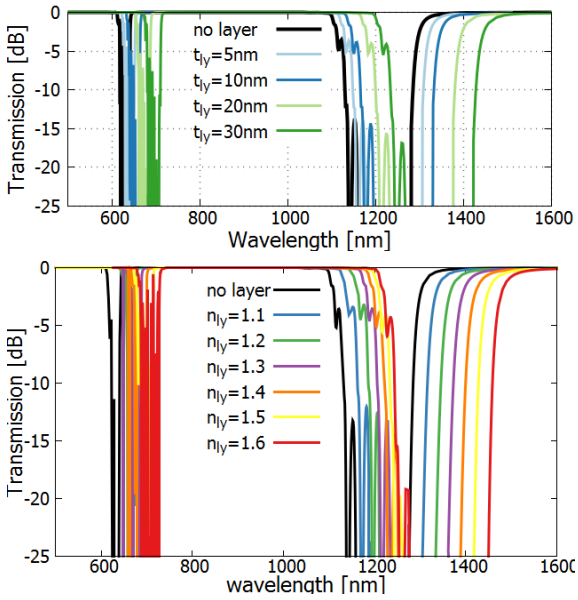

Figure 3.16: The transmission spectra of a 25 cm long TLF is displayed. The geometrical parameters are: $D_{ext} = 18\mu m$, $t_{si} = 610nm$, $\delta = 4.2\mu m$, refractive index $n_{ly} = 1.5$ and different thickness t_{ly} from $5\,nm$ to $30\,nm$ (top) and thickness $t_{ly} = 30\,nm$ and different refractive index from 1.1 to 1.6 (bottom).

Figure 3.17 summarizes the spectral shift as a function of biolayer for different refractive indexes (n_{ly} is varied from 1.1 to 1.6) in the higher wavelength region, at around of 1300nm. These results indicate that the exploitation of the features of the IC waveguiding mechanism allows the use of TLFs as refractive index sensors of layers laid down on the fiber silica surface. It is important to highlight that the sensing mechanism derives from the shift of the dispersion curves of the cladding modes determined by the additional layer and that they cause the notches in the transmission spectrum. The core modes are insensitive to the presence of the layer.

This has two main consequences:

- the sensor does not need any additional component for the detection to convert

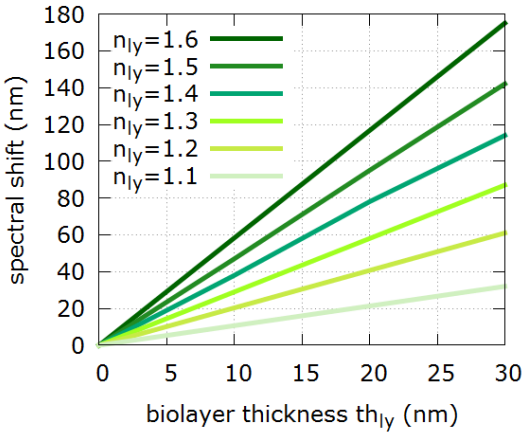

Figure 3.17: Spectral shift as a function of biolayer thickness for different values of n_{ly}

a phase variation into an amplitude variation, unlike other fiber sensors [46, 94]

- as figures 3.10(b)-(e) display, the cladding modes are very confined inside the silica and therefore they are strongly conditioned by possible layers, giving a very high sensitivity to the sensor.

Thanks to these proprieties the sensor is label-free: the device sense directly the molecule without any labels (as fluorescence molecules). According to the theoretical treatment of inhibited coupling fiber for biolayer detection, a simulation study was done to illustrate why TLF is more suitable than kagome lattice fiber for this kind of application. Figure 3.18 shows the comparison between fiber with tube and kagome lattice with a layer that emulates the presence of the biolayer after the detection process.

In particular, TLF is characterized by a simple cross-section: it presents a few numbers of nodes leading to have a loss profile less noisy. This advantage was to consider the key to use TLF respect to kagome lattice fiber for biosensing applications.

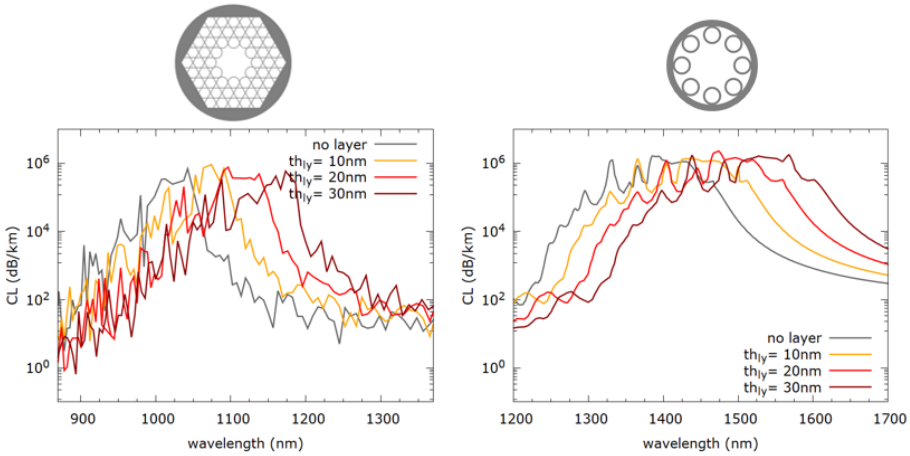

Figure 3.18: Simulation results of IC fiber as layer detector: left kagome lattice fiber; right standard TLF

3.5 Non-ideal Phenomena

Until now in this project has been supposed that the layer created in the air-silica interface is homogeneously catheterized by a flat interface. This assumption is useful to theorize the phenomena but is not sufficient. Probably the assumption made is too strong because it does not consider some non-ideal phenomena such as the non-uniform of the layer and the roughness profile of the biolayer-air interface. Moreover, the coupling between the source and the fiber is not perfectly guaranteed over the spectrum, since the beam size according to the datasheet of the manufacturer changes from 1mm to 3mm over the emitted spectrum.

3.5.1 Beam Coupling

The coupling between the source and the fiber is a phenomenon that is important to take into account. The power that the fiber can get is directly correlated with the coupling between the source and the fiber. In this project, a supercontinuum source is managed to guarantee a wide wavelength spectrum. The fibers proposed have two different mode field diameters: 31um, 27um. For simplicity, the two fiber has been coupled using just one commercial lens. The focal length of the lens can be computed with the formula (eq 3.9) making an acceptable assumption the beam is collimated:

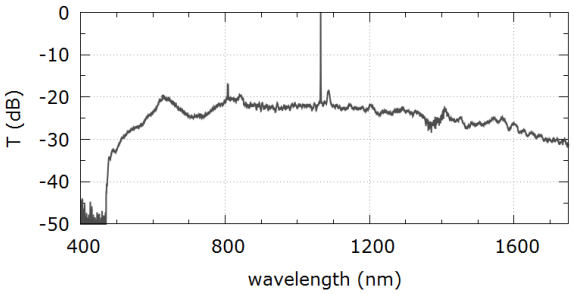

Figure 3.19: output spectrum of supercontinuum light generator, NKT

$$f = \frac{\pi}{4\lambda} dD \tag{3.9}$$

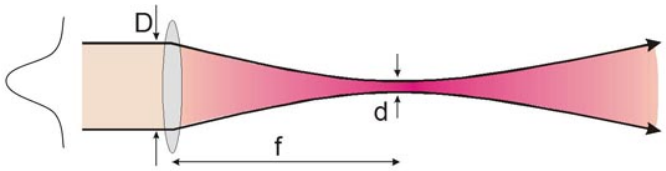

Figure 3.20: Lens for focusing a collimated Gaussian beam

where D is the beamwidth of the source, f the focal length, d is the beam in the waist. For convenience, d is considered equal to MFD of the fiber.

The specification of the light source (SuperK COMPACT NKT photonics) estimates the output beam size (collimated) of:

- 1mm at 530 nm
- 2mm at 1100 nm
- 3mm at 2000 nm

These specifications do not permit a perfect coupling between the beam generated by the source and the input of the fiber over a wide range of the spectrum. Since TLFs are multimode fibers, thought high order modes (HOMs) can be filtered out with a proper design of the tubes [95, 82], HOMs are excited when a imperfect coupling between source and fiber occurs. Both spot size and axis misalignment have examined. Sixteen different conditions of excitation ware considered by changing the spot size

from 10 μ m to 30 μ m and the axis misalignment from 0 to 0.75 the radius of the core denoted as Rco. Figure 3.21 shows the transmittance under conditions with and without a very thin biolayer of 10 nm. Despite the alteration of the transmittance spectrum and the very thin biolayer contemplate, the two groups of curves are well-separated. They allow to clearly view the redshift due to biolayer.

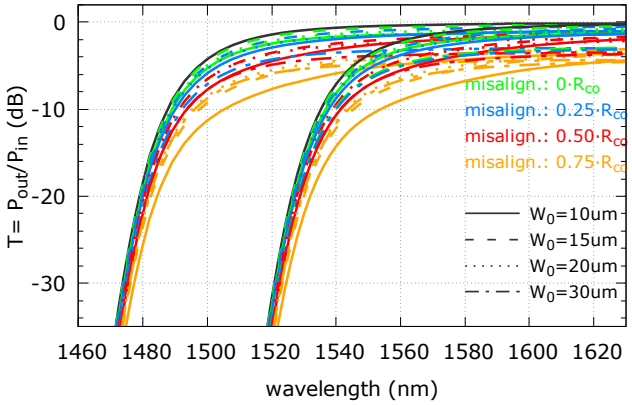

Figure 3.21: Transmission spectrum of the fiber under test with and without 10nm biolayer for different excitation conditions: a spot size (denoted with a different line style) and misalignment (denoted with a different color) of a input Gaussian beam.

3.5.2 Inhomogeneity of the Layer

Numerical simulations have been performed to understand how the inhomogeneities of the layer affect the spectrum of the fiber. Firstly an assumption was made about the distribution of the layer. The tube with a circle shape is taken as an ideal reference structure. A small relative perturbation of 1/50 is applied.

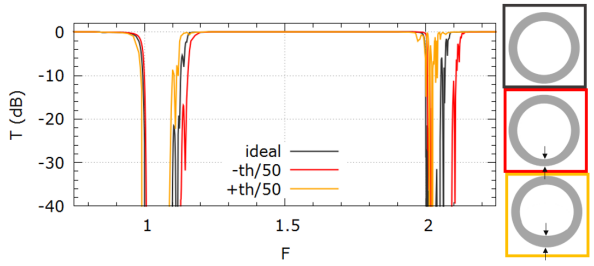

Figure 3.22: Non-homogeneous layer dependence on the azimuthal direction in a TLF. A small perturbation of th/50 is applied in each tubes. A reasonable assumption was made: a layer with the same refractive index of silica is considered

3.5.3 Empirical Estimation of the Roughness of the Biolayer

The drawing process of the fiber is highly technological. During the process, high temperatures above 1000 °C are reached where the glass medium melts. At these temperatures, the medium acts as a liquid creating a sort of waves that are replied in the fiber when it solidifies. The waves create a roughness profile of the interface between the air and silica medium. A lot of effort is spent studying how it is possible to model correctly the roughness of the silica. In particular, a model proposed by Poletti in [84] suggest an empirical formula of the surface scattering loss (SSL):

$$SSL = \eta F(\lambda) \left(\frac{\lambda_0}{\lambda} \right)^3 \tag{3.10}$$

where η is a fitting parameter that estimates the roughness profile, $F(\lambda)$ is the integral over the boundary between air-silica interface of the electrical components, λ_0 is the reference wavelength. The exponential (in this case is 3) of the equation means how is the wavelength dependence of the SSL. Figure (3.23) shows the dependence on the roughness.

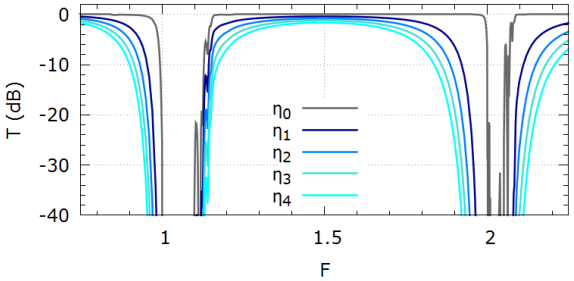

Figure 3.23: Simulated transmissivity spectrum of fiber as a function of the roughness profile according to the equation 3.10 where η_0=0, η_1=2e-3 mdB/km, η_2=4e-3 mdB/km, η_3=6e-3 mdB/km, η_4=8e-3 mdB/km

3.6 IC Fiber Loss Models

Understanding the mechanism for which light in optical fiber is attenuated is fundamental for designing new kinds of optical fiber for a specific application, but also for improving performances of the existing ones. In general, IC fiber are designed

for working from the UV [4] to IR spectrum [96] passing through the visible region [97][81] [5]. Mainly there are five contributions of leakage in IC fiber:

- absorption loss: it is due to the absorption of the material (typically silica). It has a low impact on IC fiber because most of the light is delivered by air, only a small percentage (below 1%) is guided by medium [98].
- CL: is the loss due to the geometry shape. It is computed through numeral simulations.
- SSL: is related to the surface scattering roughness of the air-dielectric interface. Since the difficulties to measure of the silica roughness profile into capillaries and to model it exhaustively, an empirical formula is proposed. Roughness is modeled as a function of the electric field at the interface, thanks to the fitting coefficient which is dependent on wavelength is it useful for roughness estimation. [99, 100, 84]
- microbending loss: is caused by random micro-bends along the fiber. As SSL contribution, it is proposed a semi-analytical formula that estimates the impact of the power exchange between core modes [85, 101, 102]
- macrobending loss: is due to the dependence on the bending deformations [103]

Chapter 4

Experimental Validation

According to the developed model exposed in section 3.4 the hollow core inhibited coupling fiber is a suitable platform to detect a small layer of deposition of biological elements. To arrange the prototyping of the sensor, an optical setup is designed to guarantee the maximum flexibility and accuracy required to perform the sensing detection. However, hollow-core inhibited coupling fibers (HCICFs) have multimode propagation and therefore coupling has an important role. The optical setup designed allows measuring the fiber with a broadband light.

4.1 Sensing Principle

The sensing principle is relative to the intrinsic properties of inhibited coupling fiber (ICF). As described in 3.4, the thickness which characterized the microstructured cladding sets the regions where the fiber works as a light deliver. In fact, according to the theory [104], the resonances generated by high coupling between core and cladding mode happen when F=m, where m is an integer number and F is the normalized frequency [82]. The alternation of resonances makes the ICF spectrum a selective optical filter wherein some regions of the spectrum the light can propagate, while in others it is attenuated by more than 40dB. Therefore, the ICF spectrum has the alternation of the notch with a high slope ($\approx 1-2dB/nm$). In fact, the sensing principle is related to the modification of the thickness of the microstructured cladding. This modification

is caused by the deposition of chemical substances, without the addition of labeled techniques as nanoparticles or dye. This result is crucial because the fiber can be considered as a label-free optical biosensor. For the sake of simplicity, the substances deposited into silica surfaces are considered as uniform thickness, represented by a uniform layer. Adding layer on the surface of silica tubes the spectrum has a shift over longer wavelength.

4.2 Fiber Characteristics

An important characteristic of this kind of fiber is the high attenuation in some bands: it allows to have a high slope in proximity to the notch. The fiber can be view as a notch filter: due to intrinsic features (see 3.3 for details) in some bands the fiber can not deliver the light since the attenuation is very high. The fibers used in these experiments were selected to have needful characteristics. The main characteristics of the fibers used are multiple bands transmission in the spectrum region analyzed. Thanks to this feature the wavelength shift can be detected in several spectrum regions. During this project two TLFs have been used with 8 and 9 tubes named respectively fiber#1 and fiber#2 (figure 4.1) which are drawn by GLOphotonics.

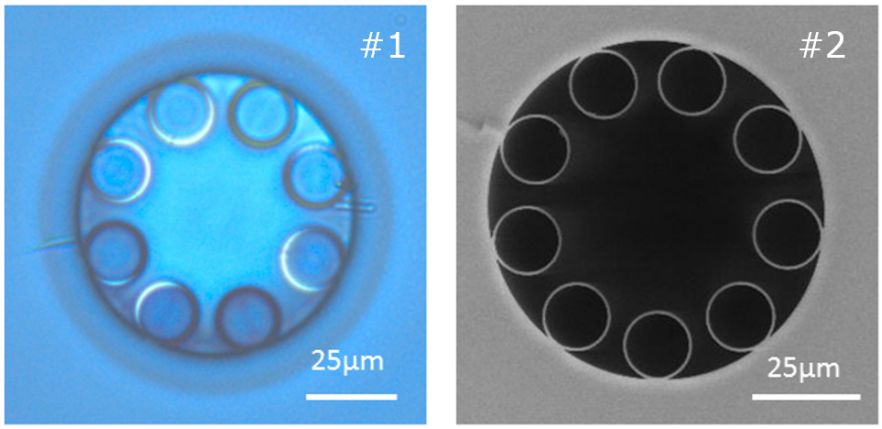

Figure 4.1: The cross-sections of fiber #1 and fiber #2

Their geometrical parameters are reported in table 4.1:

	fiber#1	fiber#2
Outer fiber diameter (um)	260	260
Core diameter (um)	39	44
Average Tube's thickness (um)	0.61	0.72
Tube number	8	9

Table 4.1: Geometrical size of TLF used for the experimental validation of the biosensor

The spectra of the fibers are shown in figure 4.2.

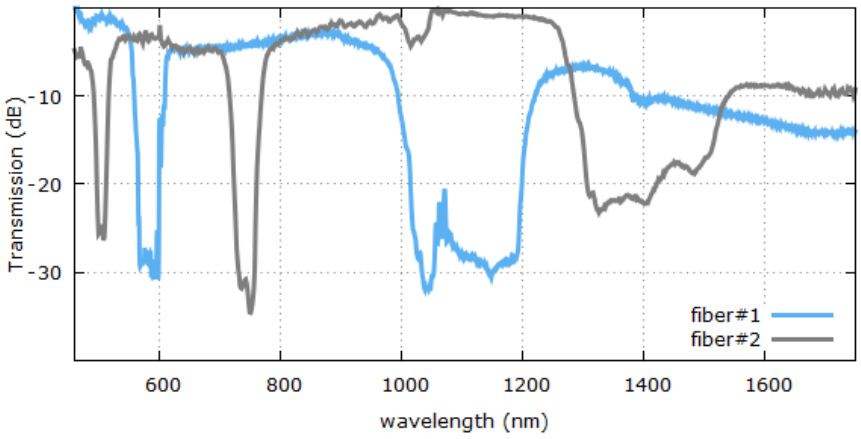

Figure 4.2: Normalized transmission spectrum of fiber#1 and fiber#2

As figure 4.2 shows fiber # 1 has 2 regions where the transmissivity is low, therefore the spectrum has 4 edges to allows the detection at around of following wavelengths: 560nm, 600nm, 1000nm and 1200nm. Instead, Fiber # 2 having 3 low transmissivity regions permits 6 edges for the detection: 500nm, 520nm 725nm, 760nm, 1260nm and 1550nm. Choosing two fibers only, it is possible to cover almost the entire spectrum from 400nm to 1400nm. Moreover, this high flexibility in selecting the wavelength is an advantage in the prototyping phase.

4.3 Chemical Procedure

The sensing mechanism as explained in section 3.4 is related to the detection of a layer of biological material (biolayer). A functionalization process is necessary to transform the fiber into a sensor: chemical and biochemical substances are the key elements to make the surface of the fiber able to capture the target molecule when

sense will happen. The fiber material is essentially pure silica (glass) and therefore it can not attract any substances. The experimental results demonstrate the feasibility to use hollow-core fiber optics as a biosensor platform. Both protein and DNA as a target molecule have given relevant results. The chemical procedure needs to sense protein or DNA is very similar. The main differences are on the probe which binds the target molecule. In particular, the proof of concept was done with the bonding biotin-streptavidin which is a well-known bonding in the literature [105], and already used for this aim [106, 107]. While for DNA sensing a complementary sequence of DNA acts as the probe, technically it is named Peptide nucleic acid (PNA). In general, the sensing platform proposed in this dissertation has been demonstrated for enzymes and for nucleic acid which are two categories of biosensor as mentioned in chapter 2. The table 4.3 summarize the two type of biosensor proposed based on IC fibers. Figure 4.3 shows the schematic representation of the chemical procedure.

	protein	DNA
probe	biotin	PNA
target	streptavidin	DNA

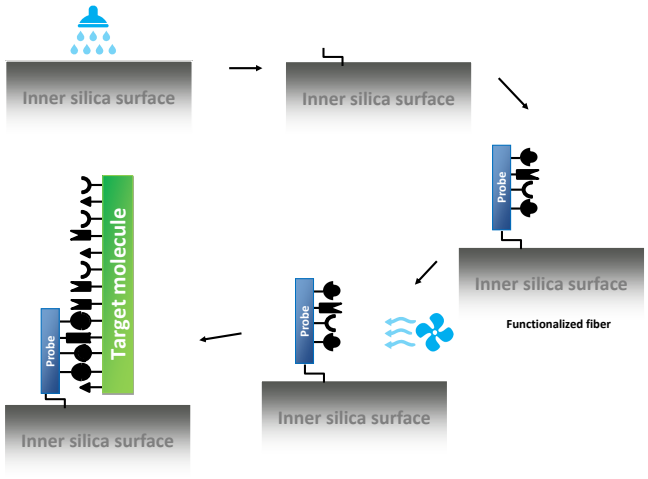

Figure 4.3: Schematic representation of the IC fiber biosensing

4.4 Hydraulic Setup

Preliminary work has been done using the biotin-streptavidin bonding to check the feasibility of the sensor. This test is frequently used for the proof of concept of the most label-free biosensor due to its affinity which is the strongest noncovalent biological interaction known, with a dissociation constant $k_d = 10^{-10}$ [108, 109, 110, 111]. In every experiment reported an in-house made system (figure 4.4) has been used to force with pressure solutions into the capillaries of the fibers.

Figure 4.4: Experimental setup for fiber infiltration

An inert gas as nitrogen (N) or argon (Ar) was used. The system showing in figure 4.4 is composed of a gas tank connected with a Teflon pipe (acting as a reservoir) through a microfluidic PEEK connector. Then, it has been connected to the fiber, thus allowing the infiltration of any solution. The pressure of 4 atm minimizes the risk of depositions of material inside the fiber, which could alter the quality of the beam and compromise the measurement.

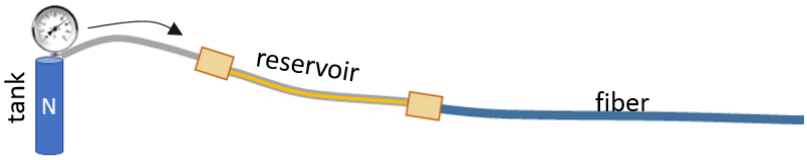

Figure 4.5: Schematic of the fluidic setup for solution infiltration

After each infiltration, a flux of argon (Ar) guarantees the removal of the liquid.

Each measurement with the optical setup shown in figure 4.7 needs a perfect coupling with the fiber. In particular, it is necessary to excite as much as possible, only the fundamental mode avoiding to generate high order mode (HoM) which could alter the quality of results. However, the short fiber length (L=0.35m), useful for the compactness of the biosensor, is not enough to consider HoM completely rejected. Moreover, the coupling could compromise the measure due to humidity in the capillaries. In light of these considerations, the liquid removal is crucial for the measurements: the difference in terms of refractive index between the air and the liquid (water) does not allow the correct coupling. Therefore, before each measurement is necessary to dry the channels with a flux of pressurized gas.

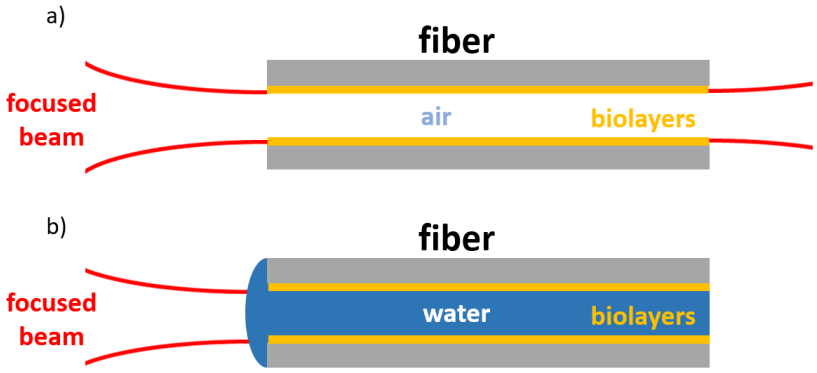

Figure 4.6: Schematic representation of right coupling a) of a fictionalized fiber b) the coupling can not be effective due to meniscus of water on the air-fiber interface

Protein Sensing: Biotin-Streptavidin

In protein sensing the functionalization procedure can be summarized into four steps:

- cleaning of the surface and activation acid with a 1:1 MeOH/HCl solution,
- APTES functionalization
- Biotin (probe) coupling in aqueous solution,
- Solution flux containing streptavidin (target) molecule

APTES deposition is an important step due to its propriety to link with the probe: if this were not present, the silica molecules would not be able to attach themselves

to the probe. All the procedures to activate the probe have been performed with high pressure of inert gas (argon or nitrogen). Microfluidic components together with hydraulic adaptors have been useful to plug the very small fiber aperture (the core which acts as a hole is about 50 μm) with the gas bottle. A proper washing has to follow all of these steps, for APTES and biotin steps an ethanol wash is enough while for streptavidin one (the target recognition step) a long aqueous wash is recommended. After streptavidin deposition, a further aqueous wash was required to eliminate all the unspecifically bound proteins. During the experiments, it is viewed that the more volatile ethanol requires less time to dissolve, while aqueous washing requires more time to remove all the water. The procedure described below needs about 2 days, however, some processes require much time to stop any reaction in the fiber. The infiltration system requires almost one hour for the infiltration of about 500 $/mu$ L of solution. The internal volume of a 30 cm long fiber is very content, 8 mu L, thus a large excess of the solution is employed. The critical steps in this procedure have proven to be APTES functionalization and biotin coupling. In the first one, a 1:20 dilution in absolute ethanol is used. A multilayer deposition was observed. This is probably due to the maintenance of an aqueous solution in the fiber derived from the previous treatment (HCl 37 % 1: 1 MeOH and washing with 96 % EtOH). The drawback is the formation of a silanic bonding at the end of the fiber. In order to remove it, cutting is needed: it loses a few centimeters of fiber. The coupling solution was injected immediately after the brief activation. In the sensing experiment 0.1 mg / mL of streptavidin solution was used in PBS (to mimic the physiological conditions), with two hours of infiltration for a total of 500 mu L. The fibers were then washed with water to remove excess streptavidin and leave to dry by rinsing nitrogen or argon for at least 2 hours.

DNA Sensing

The infiltration process is the same as previous, while the chemical steps are slightly different: the PNA infiltration is carried by DMF solution. This reason was chosen due to the absence of deposits due to salts (as HCl treatment in biotin infiltration) that could create agglomerates inside the fiber. However, the DMF respect the HCl

is denser and the removal is more crucial. The chemical step to functionalize the capillaries of the fiber are the following:

1. Activation with MeOH: HCl 1:1
2. APTES 0.1% in EtOH abs
3. Treatment with succinic anhydride 0.25M in DMF dry (Dimethylformamide)
4. Activation with DIC/NHS 0.25M in DMF
5. Infiltration of PNA in DMF dry.
6. Infiltration of DNA 100 μ M

4.5 Optical Setup

Figure 4.7 shows the schematic optical setup and (b) the picture of the optical setup.

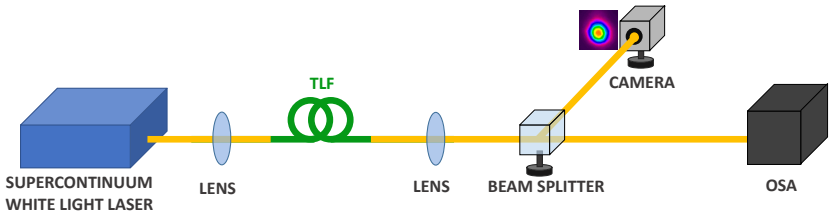

Figure 4.7: Schematic of the optical setup

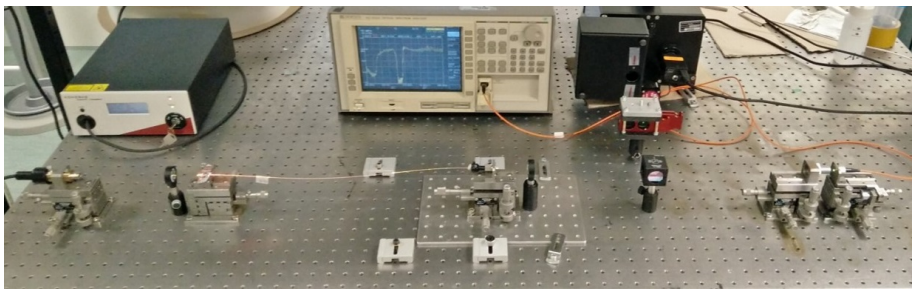

Figure 4.8: Mounted optical setup

A supercontinuum optical source is coupled to the fiber, which is suspended between 2 stages. The output beam is split by a beams splitter: the main beam is

connected to an optical spectral analyzer (OSA, Ando AQ6315a), a portion of it is monitored by a CCD camera (Point Grey GRAS-20S4M-C) to guarantee as much as possible single-mode propagation. The optical setup is essentially composed of a supercontinuum optical source (NKT) that provides a broadband spectrum from 450 to 1800 nm (3.19). Two lenses are placed respectively to focus the light into the fiber and to collect the light output the fiber. Thanks to the camera it is possible to monitor the output beam profile useful for the alignment procedure. The measurements were made in a cleanroom environment with a stable temperature. The optical setup was designed to test fibers with different lengths.

The shift expected is of the order of the thickness of the layer deposited, thus a high resolution occurs. An OSA with a resolution bandwidth of 0.5 controlled by a custom script in MATLAB code covering the range from 40nm to 1750nm has been used.

4.6 Experimental Results: Protein Sensor

In order to prove the feasibility of the platform two optical fibers with different cross-sections are employed. Figure 4.9 shows the normalized transmissivity respect with the source of the fiber before (with biotin) and after (with streptavidin) the target molecule.

According to the model developed [104] a redshift is visible in both edges. The redshift of the short and long wavelength edges of the transmission spectrum is about 24 nm and 5.7 nm, respectively. According to eq. 3.8, they correspond to layer thicknesses of 6.9 nm and 1.6 nm. In particular, a 6.9nm and 1.6nm wavelength shift are respectively in the left and the right edge. The obtained results are comparable to the size of the streptavidin molecule which is well known by crystallographic data [112]. The size of the binding biotin-streptavidin is estimated at around 6nm.

The same procedure has been reproduced with fiber#2. The results are shown in figure 4.11:

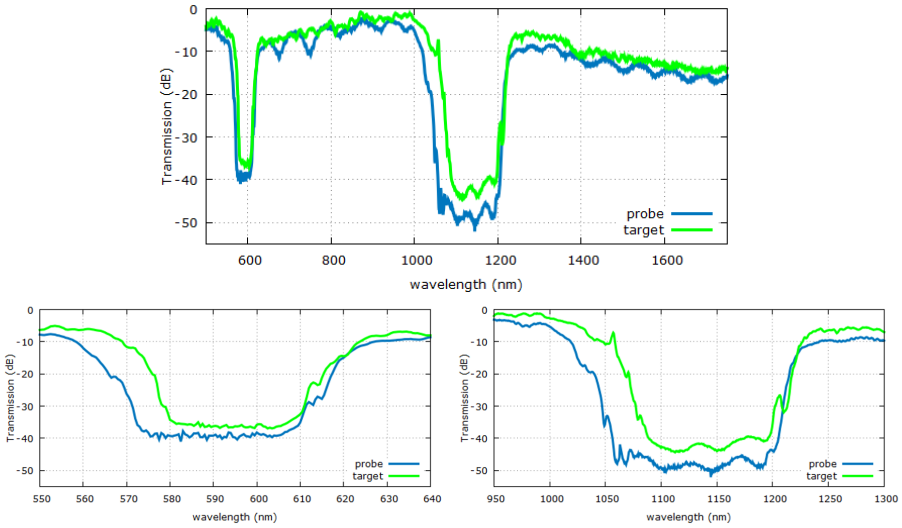

Figure 4.9: Transmissivity spectrum of fiber #1 before (with biotin) and after (with streptavidin) the detection

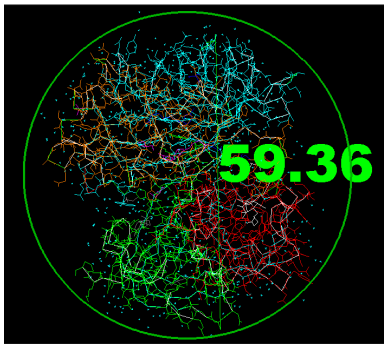

Figure 4.10: Crystallographic image of the bonding biotin-streptavidin. The numerical value is the size of the structure expressed in Armstrong

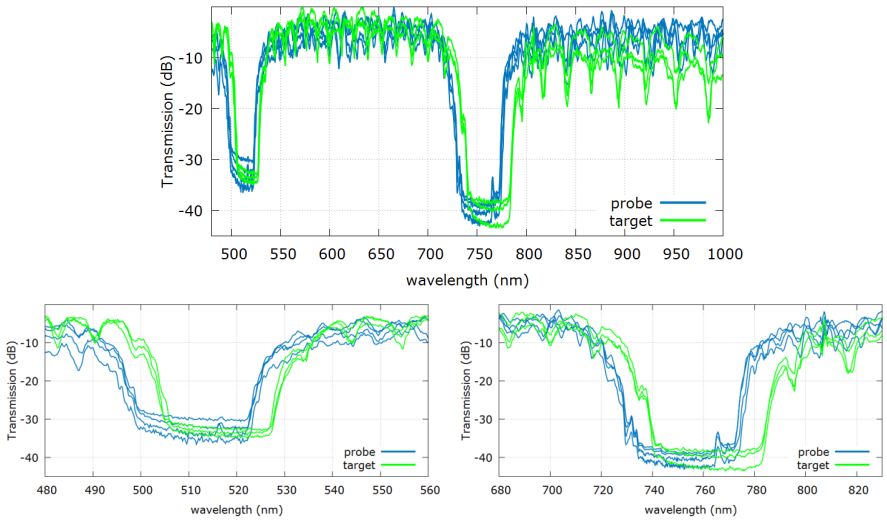

Figure 4.11: Transmissivity spectrum of fiber #2 before (with biotin) and after (with streptavidin) the detection

4.7 DNA Sensor Fiber

Since the proof of concept gave positive results demonstrating the biosensing feasibility, a PNA sensor based on the same fibers has been tested to demonstrate the feasibility of the entire platform and the theory developed behind. The probe in this scenario is peptide nucleic acid (PNA): a complementary sequence of the DNA target molecule. PNA is an artificially synthesized polymer with the same features of the DNA. The main concern of the length of the PNA is to guarantee the specificity: it is defined as the affinity of binding to one relative to the other targets [113]. The DNA used in this experiment is the genetically modified soybean which is well-known and widely diffused. The PNA was prepared by the chemical departments of Parma by Andrea Rozzi and its supervisor Roberto Corradini.

4.7.1 Label-based Fiber for Biosensing

A useful feature used was to decorate the DNA with fluorophore allowing both labeled and label-free sensing. Since the PNA-DNA bonging is weaker respect to biotin-streptavidin one, it was decided to check the presence of the analyte through labeled-based techniques. To prove the feasibility of the fiber biosensor based on inhibited coupling fiber a fluorescent test has been done. In particular, the fluorescent molecule Cy3 has been used. Figure (4.12) shows the relative intensity of absorption (dashed line) and emission (solid line) over the wavelength spectrum. The absorption of the Cy3 molecule is around 554nm and the emission on 568nm. The DNA used is linked with a Cy3 to check the sensor working principle. The test was done to demonstrate two assumptions: first, the fiber can attract DNA inside the channels; second, the variation of the concentration of the probe (PNA) changes the DNA detected.

4.7.2 Experimental Results: DNA Sensor

Another test was done to demonstrate the reusability of the sensor. Since the bonding between PNA-DNA is not so strong, therefore is possible to break through the washing of the Urea solution. After washing urea for one hour and a proper drying for about one hour, the spectrum partially returns at the position of PNA as shown in figure

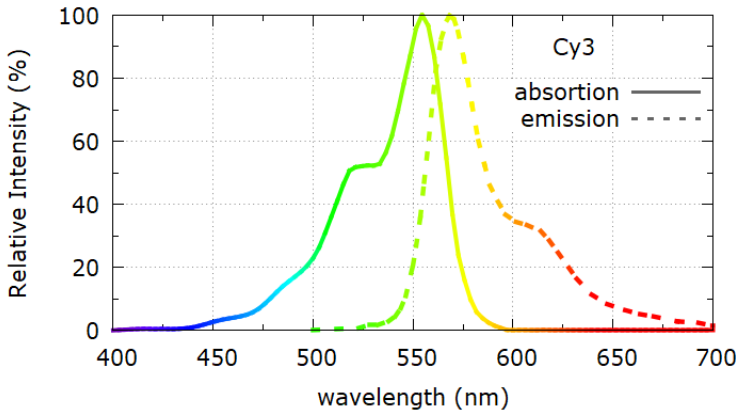

Figure 4.12: Absorption (solid line) and emission (dashed line) spectra of Cy3

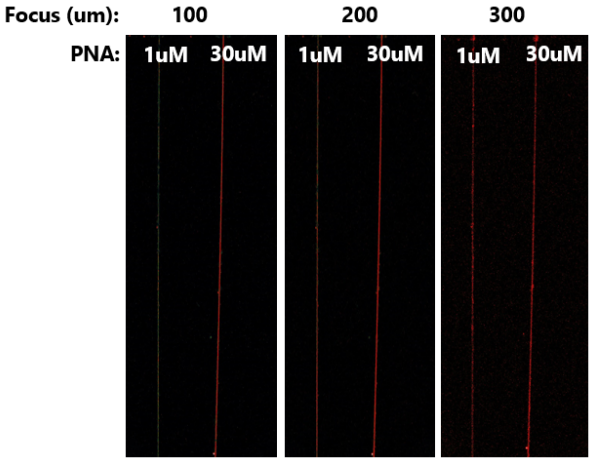

Figure 4.13: Fluorescent images of optical fiber with labeled DNA. The comparison was done using a different concentrations of PNA: 1μ m and 30μ. Three different focuses are considered

4.15.

Thanks to a camera the near field profiles are recorded to avoid, as much as possible, the excitation of high order modes. Figure 4.16 shows the profile of 25 cm long with probe and target measurements.

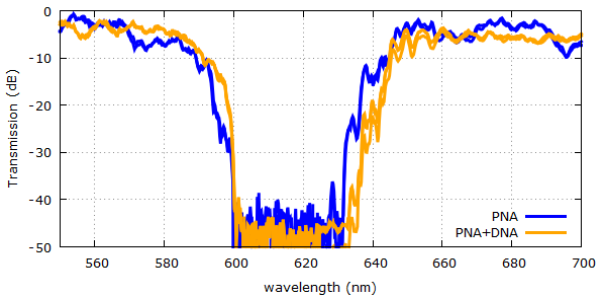

Figure 4.14: Transmissivity spectrum of fiber #1 before (with PNA) and after (with DNA) the detection

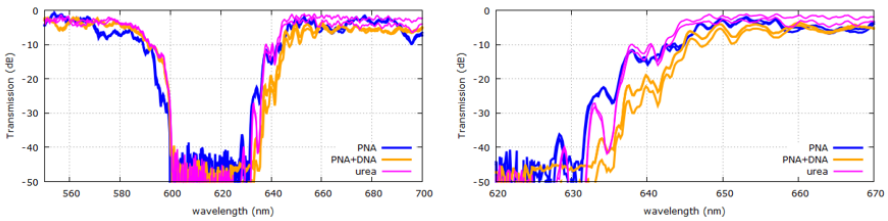

Figure 4.15: Transmissivity spectrum of fiber #1 with PNA, DNA and Urea to remove the layer of DNA

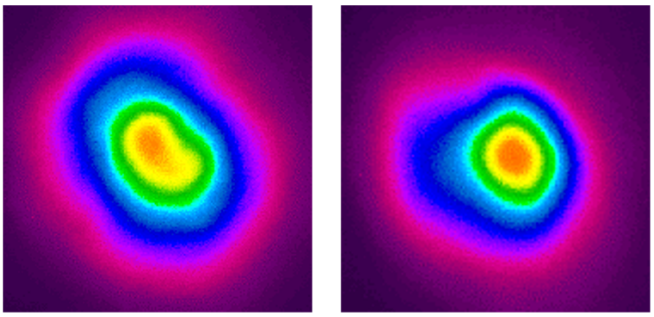

Figure 4.16: Near-field experimental profiles recorded at the 30 cm long fiber #1 output with probe (left) and target (right).

Chapter 5

Fiber Design

During my Ph.D., I participated in several projects to improve the performances of inhibited coupling fibers which involved the GPPMM group at the research laboratory XLIM in Limoges, France. The peculiar geometry of IC fibers offers a high degree of freedom to arrange unusual structures. This feature, combined with the technical ability of the group, allows reaching technological requests in the optical fiber applications.

5.1 Asymmetric Fiber

Understanding the cladding proprieties is fundamental for fiber design, in particular, for inhibited coupling one. For this kind of fiber, the cladding proprieties play an important role to know due to the waveguiding mechanism [82, 86, 81]. The novelty published in [114] was to demonstrate high order mode can propagate suppressing the fundamental one. This is suitable without using any filter or other additional components. In particular, in this section, it will be shown how it is possible to suppress some guided mode i.e. the fundamental one just by acting on the arrangement of the tube surrounding the cladding.

5.1.1 Simulation Results

According to step-index optical fiber theory, pseudo-modes $LP_{\nu\mu}$ mode with two indexes: ν and μ which are the radial and the azimuthal number respectively related with the maximum in radial and azimuthal direction of the normalized electric field **intensity**. In particular, the fundamental mode has a intensity profile similar to LP_{01} where $\nu = 0$ and $\mu = 1$. It is characterized by the highest effective index and lowest confinement loss (CL). Following mode to LP_{01} are LP_{11a}, LP_{11b} and LP_{21}.

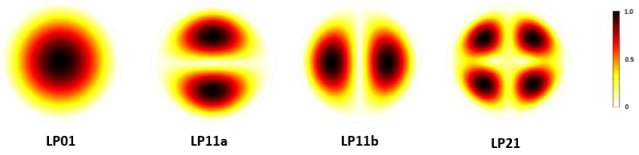

Figure 5.1: Electric field amplitude profiles of $LP_{\nu\mu}$

These modes are noted as high order mode (HoM). Other modes, with higher ν and μ, are reasonably neglected in this study. In the study, a standard TLF with 10 tubes is considered as a reference, here namely noGapTLF. Two other TLF is considered for the proof of concept: in the first one, two large gaps defining an angle of 180°, obtained by removing 2 tubes in horizontal plane (2gapTLF), while the second fiber four large gaps are open every 90° where 2 others tube are removed in the vertical plane (2gapTLF). As the *gap* is defined as the larger distance between the tube, while as d the shorter distance between tubes 5.2. Obviously, in the case of noGapTLF gap= d. The larger gaps in 2gapsTLF and 4gapsTLF are respectively $gap = 20.2\mu m$ and $12.3\mu m$. To compare their geometric sizes as core diameter (2Rco= $45\mu m$) and tubes dimensions (outer diameter D=$15\mu m$ and thickness t=750nm) are kept constant. Since the n-fold symmetry is changed, this type of fibers has been improperly called asymmetric fibers.

The mechanism which makes possible to recombine the hierarchy of minimum loss of $LP_{01}, LP_{11a}, LP_{11b}, LP_{21}$ can be understood displaying the map of radial Poynting vector p_r, which is defined as:

$$p_r = \frac{1}{2p_z}\vec{E} \times \vec{H} * \hat{r} \tag{5.1}$$

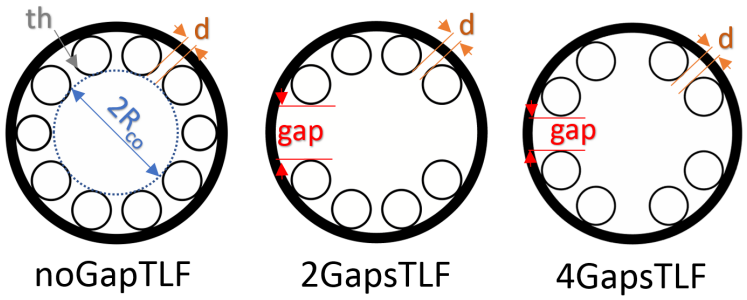

Figure 5.2: Cross-section of examined fiber

The radial Poynting vector gives the spatial distribution of the leakage along the transverse direction [81]. The flux of power density along the radial direction is described by the normalized radial component of the Poynting vector, pr, given by Eq. 5.1, where $\vec{E}$ and $\vec{H}$ are the electric and magnetic fields of the mode, r is the radial unit vector, and pz the maximum value of longitudinal component of the Poynting vector [81, 114]. The results of this theoretical study are shown in figure 5.3, where the radial Poynting vector (at the wavelength of 1000 nm, close to the minimum of CL) is displayed in a map in the logarithm scale: lighter color means low loss.

Considering noGapTLF and it is $LP11a$ mode lighter color is along the horizontal line meaning a low amount of leakage in this direction. Opening two larger gaps at the horizontal line (where the leakage flux is low) 2GapTLF are considered. Its Poynting vector map of LP_{11a} is quite similar to noGapTLF. Moreover, the same concept is applicable for LP_{21} 2GapTLF and 4GapTLF have an analog color map, meaning a comparable leakage flux.

In the picture 5.4 are shown the simulated cross-section and the loss distribution of each fiber design. All these fibers have almost the same refractive index, because of the low changement of the core size. On the contrary, the loss hierarchy has dramatic alterations from noGapTLF to 4gaps. In particular, the mode with the lowest CL for noGapTLF is LP_{01}, as expected, but it is not the same for the other two. The CL of LP_{11a} has more than 1 decade from LP_{01} in 2gapsTLF. It entails that, for 2gapsTLF, CL LP_{11a} mode is calculated to be 33 dB/km at 1000 nm – not so far from the loss of the same mode in noGapTLF (12 dB/km). Moreover, LP_{21} around 1040 nm has the lowest CL. From the results obtained it is visible that LP_{11a} mode

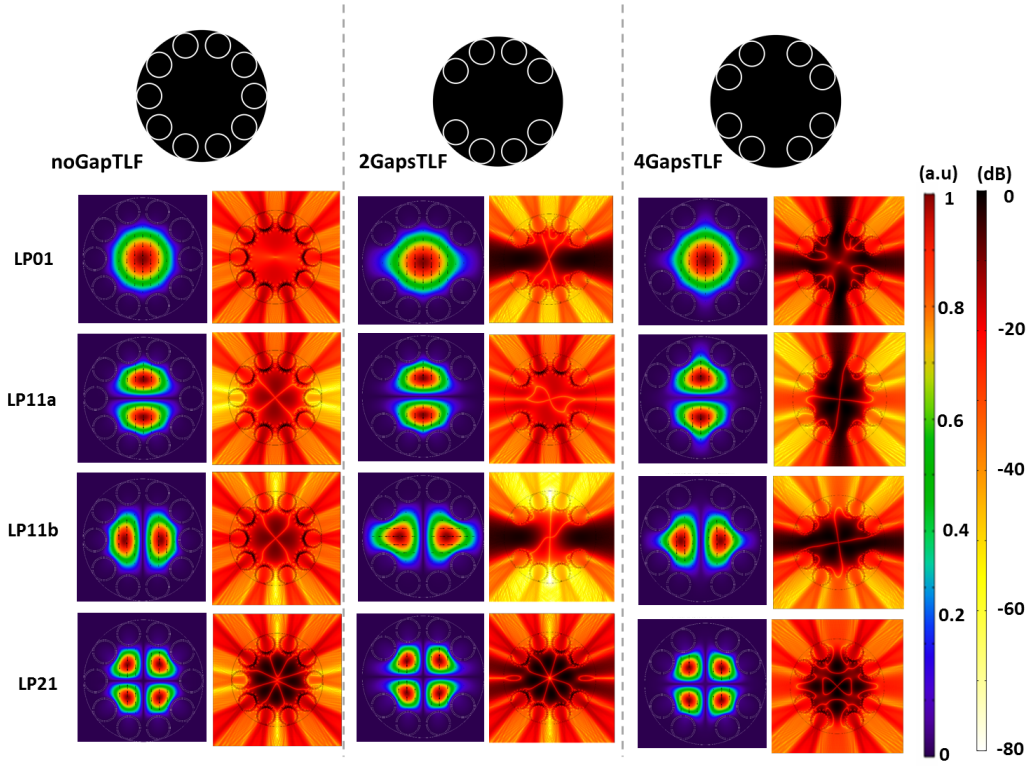

Figure 5.3: Representation of normalized electric filed distribution and the radial Poynting vector of LP_{01}, LP_{11a}, LP_{11b} and LP_{21} modes of noGapTLF, 2GapsTLF and 4GapsTLF configurations. Electric filed distribution is displayed with normalized scale, while the radial Poynting vector is normalized and it has displayed in a logarithmic scale

is less loss-sensitive in 2GapsTLF than in 4GapsTLF. On the contrary, LP_{21} mode in 4GapsTLF is less loss-sensitive than 2GapsTLF. This feature is coherent with the radial Poynting vector.

Distributions are shown in figure 5.3: in 2GapsTLF the mode with a minimum loss is LP_{11a} because is the only that has a zero line of the normalized intensity profile along the gap. LP_{11a} is the only mode that does not sense the gap alteration from noGapTLF to 2GapTLF. The same reason for LP_{21} in 4GapsTLF. Observing the mode distribution in figure 5.3 noGapTLF has modal content as a reference, modes are well confined in the core by the surrounded cladding and the radial Poynting vector maps show light colors meaning low leakage in the radial direction. In 2GapTLF LP_{01} and LP_{11b} have black flows in the map of the radial Poynting vector, indicating an

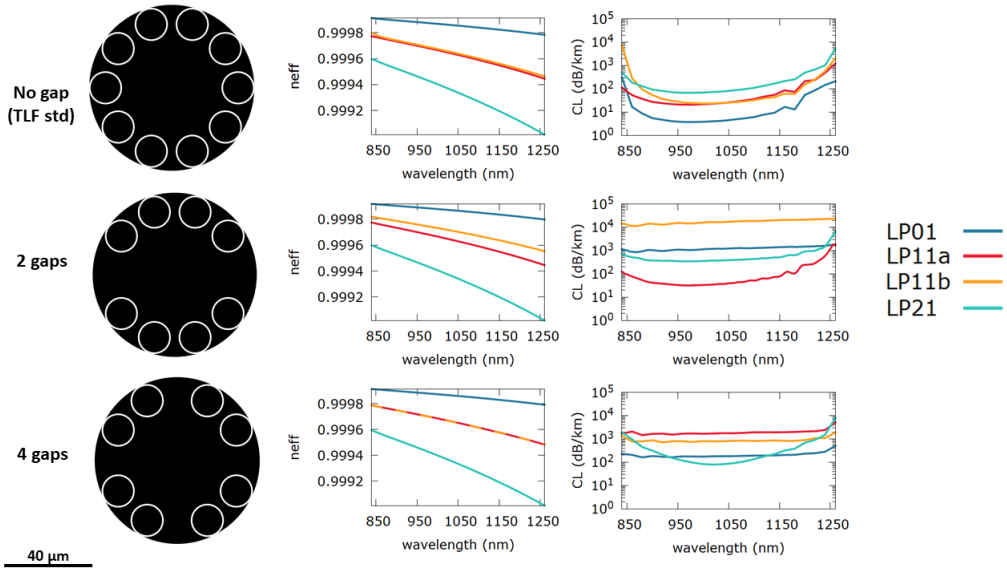

Figure 5.4: Schematic diagram of the cross sections of the analyzed fibers; The charts represents the effective refractive index (neff) and the CL as a function of the wavelength for LP_{01}, LP_{11a}, LP_{11b} and LP_{21} modes.

increase of the leakage in that direction. In 4GapsTLF the only mode having a similar radial Poynting vector respect to noGapTLF and 2GapsTLF is the LP_{21} which has a similar loss than LP_{21} noGapTLF. In other words, in 2GapsTLF LP_{11a} is the first mode in the hierarchy, while in 4GapsTLF the first one is LP_{21}.

Moreover, a study was done to understand in the 4GapsTLF the role of the bigger gap (gap) respect the gap between tubes (d). Figure 5.5 shows three different configurations $F\#1, F\#2$ and $F\#3$ where d=3.5μm is kept constant, while gap is changed. In particular, $gap\#1 = 12.6\mu m$, $gap\#2 = 10.16\mu m$ and $gap\#3 = 7.74\mu m$, thus the ratio $gap/d\#1 = 3.6$, $gap/d\#2 = 2.90$ and $gap/d\#3 = 2.21$.

As shown in figure 5.5 the $F\#1$ has a minimum loss at around wavelength 1020 nm. Increasing the ratio gap/d $LP_{01}, LP_{11a}, LP_{11b}$ progressively increase theirs loss whereas LP_{01} loss are just slightly affected. In figure 5.5 the gap dependence for each mode is shown separately.

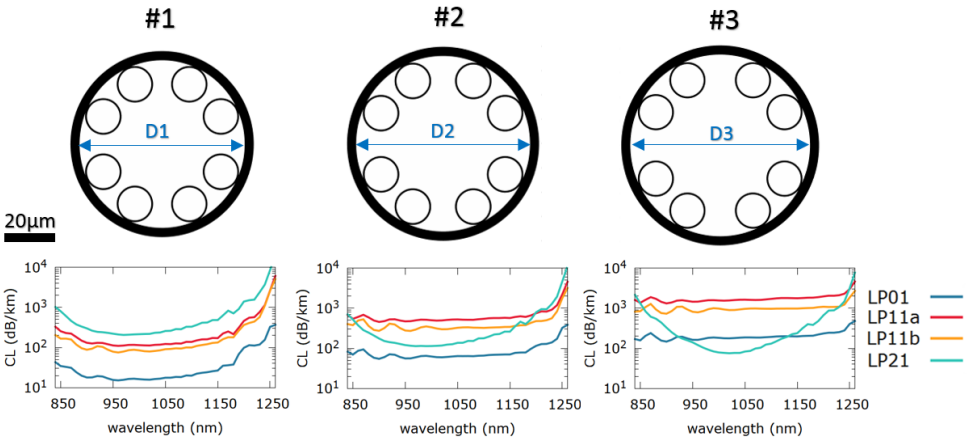

Figure 5.5: gap/d dependence of a 4GapsTLF. Cross-section and CL of LP_{01}, LP_{11a}, LP_{11b} and LP_{21} modes are reported. D1= 68.5μ m, D2= 71.75 μ m, D3= 75 μ m

5.1.2 Experimental Results

To experimentally verify the results obtained in the theoretical analysis shown in the previous section two different fibers have been drawn by GPPMM at XLIM in Limoges. Here, we index to the fabricated fibers as Fa and Fb to avoid confusion with the simulated ones. Fa structure has 2 larger gaps where they are defined by an angle of 180°. While Fb has 4 larger gaps at 90° between each other. In figure 5.7 a) is shown the cross-section of Fa where gap=17 μm and d= 4 μm; while in figure 5.8 b) is shown Fb, where gap= 9.2 μm and d= 3.4 μm. Experimentally, several cut-backs were necessary to compute the loss in each fiber as figures 5.7 b) and 5.8 b) show.

Experimental loss are shown in figure 5.7 b) has a good agreement with simulated mode. In particular, at the wavelength around 1000nm, there is a minimum of loss. Thanks to a camera, near field profiles superimposed to fiber cross-section are recorded at different lengths figure 5.7 c). The results obtained are coherent with the theoretical analysis: Fa have a high rejection of LP_{01} and LP_{21} modes leading to the LP_{11a} to be the mode with the lowest loss. Length of 3.2 m is sufficient to have LP_{11a} mode still present.

Analogously, figure 5.8 b) shows experimental and simulated loss of Fb. Figure 5.8 c) are reported near field profiles superimposed to the fiber cross-section to help

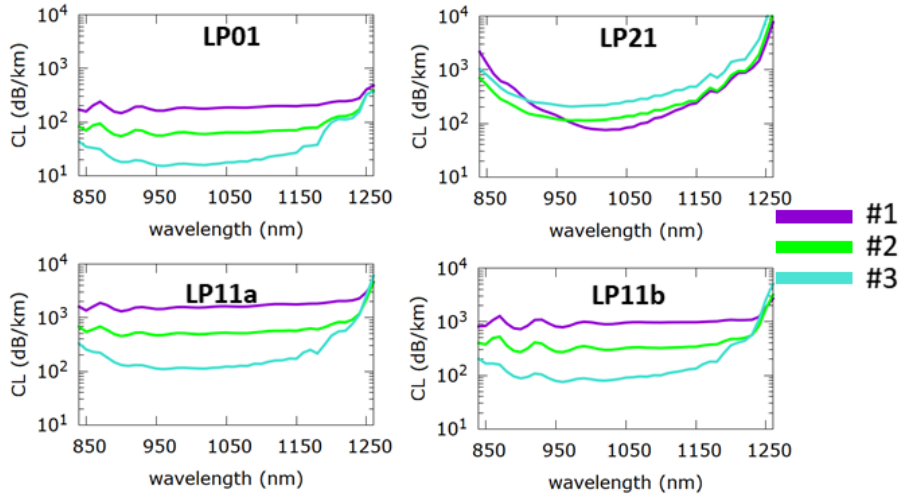

Figure 5.6: Confinement loss comparison of LP_{01}, LP_{21}, LP_{11a}, LP_{11b} of three 4GapsTLF fiber.$F\#1$, having a high rejection ratio of the LP01 and LP11 mode, allows the LP21 mode to have the lowest CL

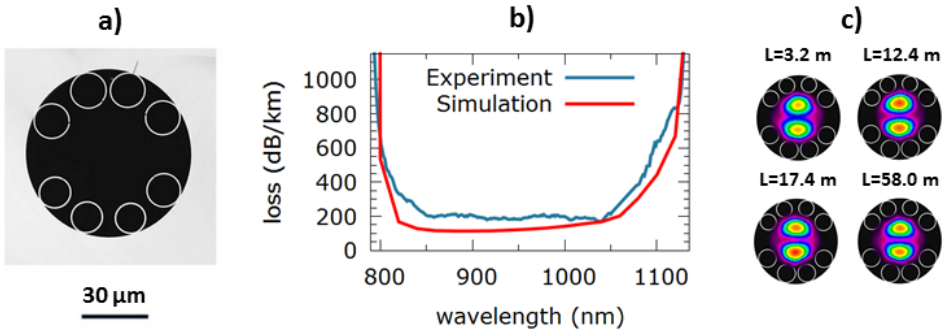

Figure 5.7: a) Fa cross-section b) experimental and simulation loss c) near filed profiles at different fiber lengths

the visualization. The measured loss for the LP_{21} mode in Fb was quantified as 300dB/km around the wavelengths of 1000 nm. Therefore, it is possible to state that the experimental results confirm the simulated model. In fact, fiber Fa is able to propagate LP_{11} filtering out LP_{01}, while Fb can propagate LP_{21} filtering out LP_{01} , LP_{11a} and LP_{11b}.

In conclusion, the theoretical and experimental investigation of the properties of IC TLF with modified cladding structures is analyzed. A strategic modification of the azimuthal position of the tubes allows altering the mode losses hierarchy. To study this new concept, we investigated two novel fibers with modified cladding structures,

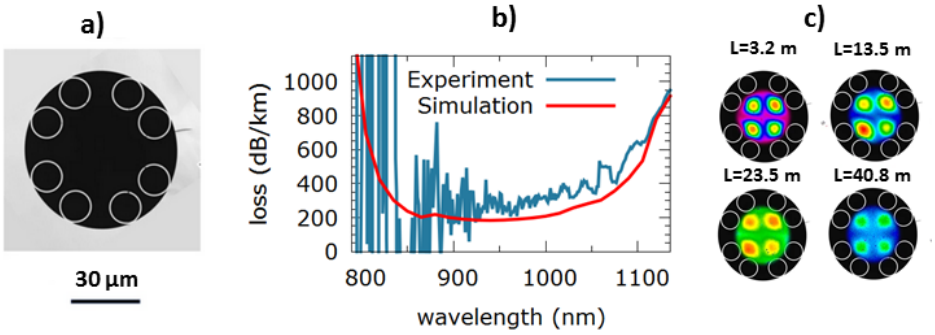

Figure 5.8: a) *Fb* cross-section b) experimental and simulation loss c) near filed profiles at different fiber lengths

which support the propagation of LP_{11} and LP_{21} modes. We think this novel concept can be useful for several applications where the mode field distribution plays a crucial role such as hollow-core fiber based on atom optics, atom-surface physics, sensing, and nonlinear optics [86].

5.2 Hybrid Fiber

Hollow-core inhibited coupling fiber has a lot of interest due to its features such as the possibility to guide the light into a hole. In the last years, researchers are trying to overcome the limits of improving performances. As discussed in the previous section one of the most important figures of merit of a fiber is the loss over the distance. IC mechanism fibers are developed with different cross-sections typologies (such as kagome figure 3.2 a), type-cone 3.2 b) c), TLF 3.2 d), nested TLF 3.2 e), conjoined 3.2 f)).

The research carried on in the last years was devoted to proposing a new kind of geometry cross-section able to reduce the leakage. In this section, the advantage to combine two typologies of IC fiber kagome lattice and TLF is proposed, analyzed, and experimentally demonstrated. Both kind of fibers are studied in several papers,[118] [87] [119] [81] in particular the kagome fiber was the first IC fiber proposed in the literature by Benabid et al. [88], while TLF, due to its simplicity geometry, is continuously studied improving the performances. The study is focused on the demonstration that TLF surrounded by an additional microstructured cladding, as kagome lattice,

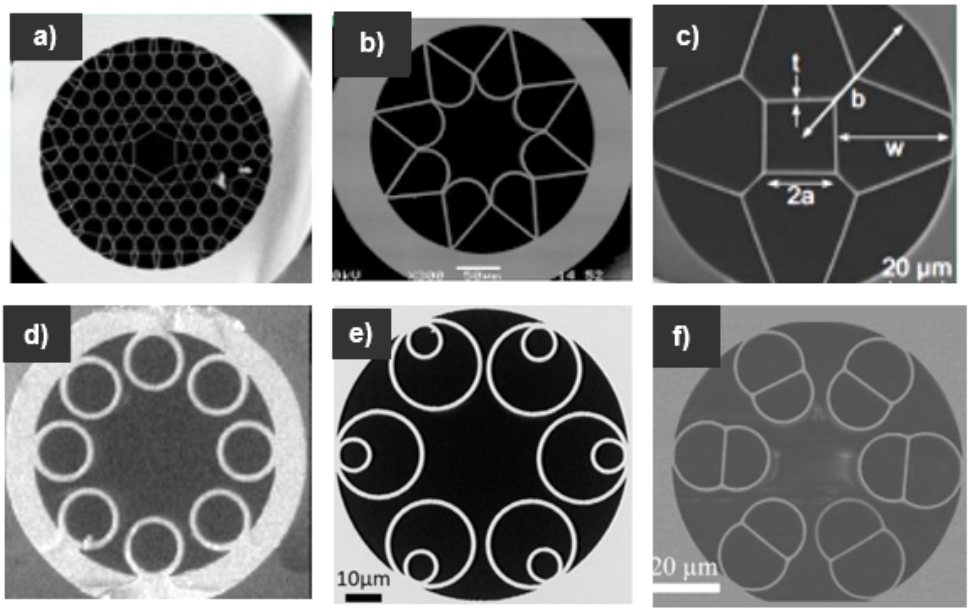

Figure 5.9: SEM images of hollow-core inhibited coupling fibers: a) kagome fiber [87] b) cone-type fiber with hypocycloidal core-contour [115] c) cone-type fiber with square core-contour [116] d)Tube lattice fiber [96] e) Nested tube lattice fiber [85] f) Conjoined fiber [117]

reduces leakage contribution.

5.2.1 Simulation Results

The fiber is firstly investigating by considering an ideal version composed of kagome fiber and suspended TLF which defines the core. Although this structure is not achievable, the results obtained can be useful for a new type of IC fiber. Following, the topology proposed will be named as ideal hybrid fiber as shown in figure 5.10. *gap* is identified as the distance between the tube and kagome lattice.

In order to understand the role of kagome lattice, a comparison with kagome fiber and a standard TLF with the same core diameter of 35 μm was as shown in figure 5.11. The comparison has the aim to understand the impact of kagome lattice to block the leakage. As shown in figure 5.11 CL of ideal hybrid fiber is more than 3 decades low with respect to the others.

The reduction is considerable also respect to TLF surrounded by air, where the tube is suspended in the air. TLF surrounded by air has comparable loss than stan-

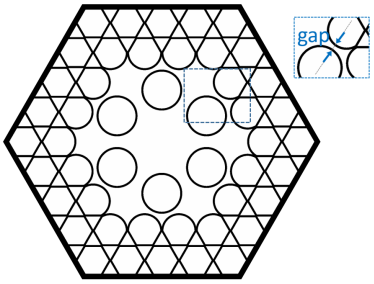

Figure 5.10: Cross-section of the fiber topology proposed: hybrid fiber. Its cladding is composed of the combination of TLF and kagome lattice

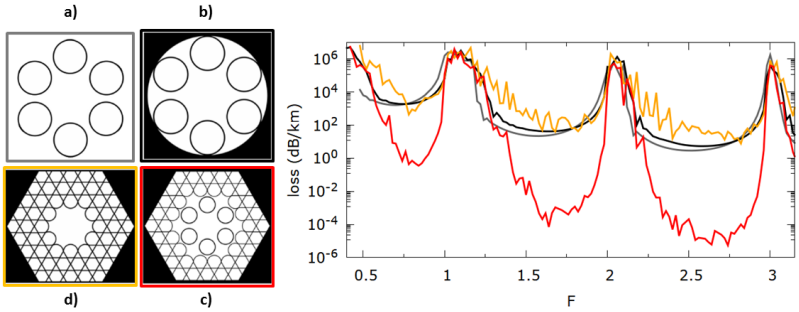

Figure 5.11: Confinement loss comparison of 4 typologies of fiber cross section: a) TLF surrounded by air, b) standard TLF, C) hybrid fiber, D) kagome fiber

dard TLF. Therefore, the impact of homogeneous silica in standard TLF has a low impact. Another way to demonstrate the role of kagome lattice is been studied progressively removing the kagome lattice as shown in figure 5.12.

Integer values of ξ correspond to a finite number of holes rings in the kagome cladding; ξ= 0 corresponds to no kagome cladding. Comparing the corner cases: $\xi = 0$ and $\xi = 2$ the confinement loss difference is more than 3 decades. The role of the kagome lattice is still considerable until complete presence hypocycloid cladding, where $\xi = 0.5$. When ξ became closer to zero value the second cladding contour is not well defined, creating nodes that add resonances with cladding modes ending with increasing losses. This phenomenon can be explained considering the radial pointing vector 5.1, useful to graph the leakage across the radial direction 5.13. The figure 5.1 shows with a colored map the flux of the leakage through radial direction: darker color means high leakage. It is interesting to note that $\xi = 1$ and $\xi = 2$ have almost the same level of leakage loss.

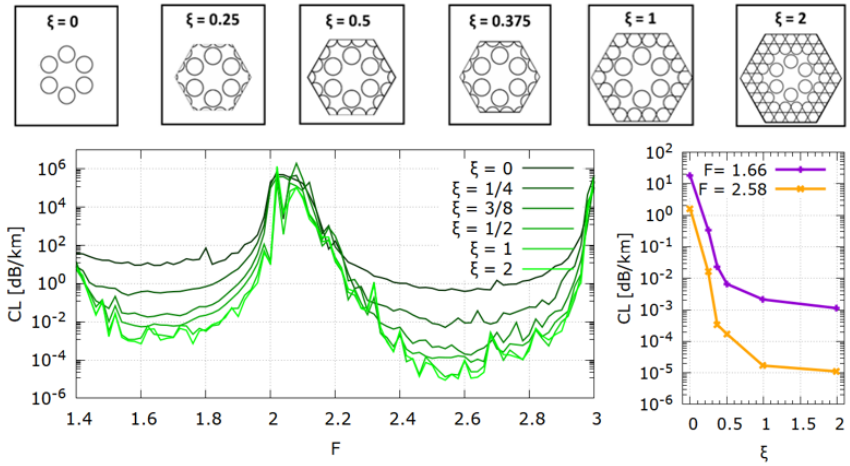

Figure 5.12: Representation of the kagome lattice dependence in hybrid fiber. A study to vary the parameter ξ is reported

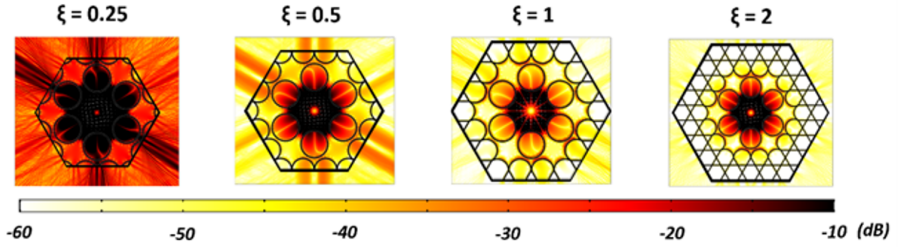

Figure 5.13: Map of Radial Poynting vector at F=2.58. From left to right the increased of kagome lattice in a hybrid fiber: $\xi = 0$ (no lattice) and $\xi = 2$ (2 rings)

This strong improvement concerning single cladding hollow-core fibers is mainly due to TLF and kagome cladding one disjointed. When the gap between the tube and the lattice surrounded is progressively reduced to zero the CL rises sharply. At gap = 0μm the leakage can flow from TLF to kagome lattice guided by silica. Figure 5.14 shows the CL varying the gap from 0 (TLF and kagome lattice are tangent) to gap 12 μm where kagome is very far from TLF. In figure 5.14 can be easily noticed that a threshold effect happens in the proximity of gap = 1μm, it confirms what said before. Until two structure remains separate the kagome lattice blocks very well the leakage flux. At gap=0 they create a single structure, therefore the leakage can flows increasing CL.

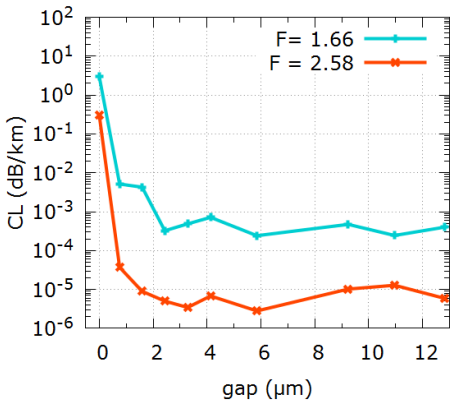

Figure 5.14: Gap dependence in the loss of hybrid fiber

5.2.2 Experimental Results

The potentiality shown by simulations led to fabricate the fiber. The cross-section shown in figure 5.15 has been obtained by stack-and-draw technique [120] [121]. The drawn fiber has a core diameter of 37.1 μm, while the average inner tube diameter of 23 μm and thickness 1.27 μm. Their ratio $D_{tubes}/D_{core} = 0.62$ is closer to 0.68 which is the theoretical value where there is the maximum LP_{11} mode rejection [95]. The struts composing the kagome lattice have an average thickness of 720 nm, while struts making the connection with kagome 365 nm.

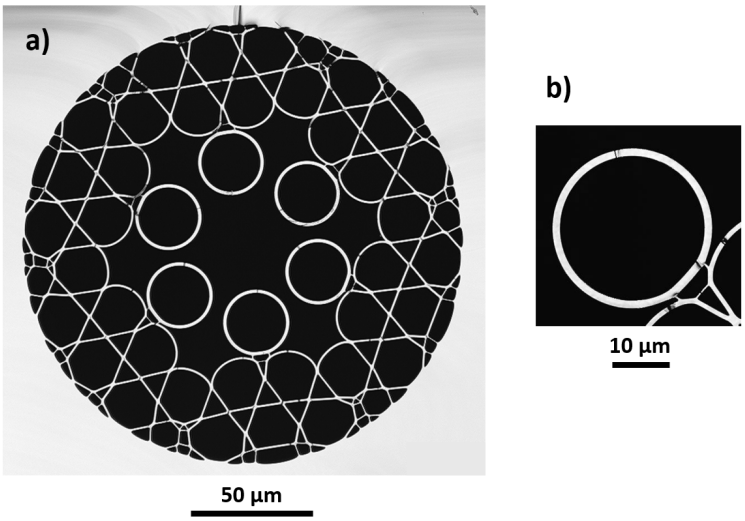

Figure 5.15: a) Cross-section of the drawn hybrid fiber b) a details of a tube and its struts

In order to estimate the leakage, a finite element method software (COMSOL Multiphysics) has been used to simulate the loss contribution. Figure 5.16 shows the loss measured with cut-back technique.

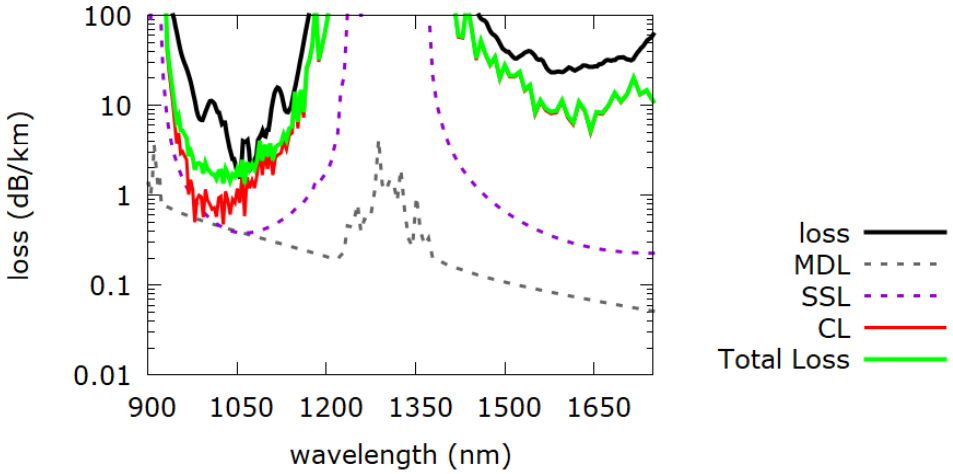

Figure 5.16: Comparison of experimental and simulated loss spectra

To estimate the loss measurements CL, MDL and SSL are considered. In particular, as mention in section 3.6, MDL and SSL are computed through a semi-analytical formula. However, a good agreement between experimental loss and the total simulated loss is reached. A minimum loss of 1.61 dB/km is in correspondence of wavelength 1057nm. This result is surprising considering the experimental results obtained by conjoined fiber (at now one of the most interesting configuration topology) where the minimum loss of 2 dB/km is reached at 1512nm [89].

Chapter 6

Final Considerations

The work described in this doctorate thesis aimed at the proof of concept of a new kind of optical fiber biosensor based on hollow-core inhibited coupling fiber. Thanks to a proper functionalization, the inner surface of the fiber capillaries is coated with a probe layer able to selectively bond only the target molecule.

Thanks to the inhibited coupling waveguide mechanism, the fiber biosensor proposed is very sensitive even with thin layers and a low refractive index. Moreover, it does not require any additional component of the transducer such as Bragg gratings or amplification techniques such as nanoparticles. After the functionalization of a piece of the fiber of tens of centimeters long, the sensing procedure consists of a liquid infiltration of the solution containing the target and measurements of the transmissivity of the spectrum. The microfluidic and optical setup required is both cheap and simple to use. Hence, since the cost of the device is strongly dependent on the cost of the fiber, one of the main advantages of the platform proposed is its inexpensiveness. Actually, these types of fibers are for research purposes and therefore they are not produced in large volumes: however, since the applications of hollow-core fiber are in numerous fields ranging from medical to industrial applications, it can be stated that their unit cost will drop dramatically.

Theoretical and experimental analyses are in agreement: a spectral redshift of the transmission spectrum has been successfully measured when the probe selectively forms a biolayer with the target molecule.

The principal is also confirmed by the numerical model. A brief review of non-ideal phenomena about the biolayer can be useful for the modeling of the sensor.

In the theoretical study, various possible scenarios of the sensing measurements have been taken into account. Since the estimation of thickness and the refractive index of the biolayer is difficult, a wide range of configurations is considered. Moreover, a possible dependency on the distribution of the biolayer inside the fiber and its roughness has been examined. In both studies, an asymmetrical shift between the right and the left edges of the transmissivity spectrum is expected.

The experimental results demonstrate the sensing of two different target molecule: a protein (streptavidin) and a nucleic acid (DNA of genetically modified soybean). The measurement of the transmission spectrum before and after the infiltration showed the presence of the target.

Moreover, the technique is not restricted to particular wavelengths. Thanks to the intrinsic proprieties of inhibited coupling fiber, the operating wavelength is tuned by the thickness of the silica structure. Therefore, proper designing of the geometry of the fiber allows selecting the suitable wavelength. In the last years, the technology of inhibited coupling fibers has been becoming more and more mature.

Although other several works are necessary to measure the sensitivity and sensibility of the biosensor, this platform can be considered a valid candidate for biosensing.

The research activity has been also devoted to improve and control the transmission properties of HC-IC fibers. In particular, two novel types of IC are proposed. Thanks to asymmetric fiber arranging tube cladding it is possible to change the mode hierarchy, while hybrid fiber composed by the combination of TLF and kagome lattice has shown very low loss.

Appendix A

Appendix

A.1 Modelling of Fabricated TLF

The importance to reconstruct a cross-section to simulate a most accurate version of the real fiber cross-section is a crucial issue. A crucial point is the correct estimation of the thickness of the microstructured cladding [122]. A mismatched thickness can cause a shift in the wavelength spectrum as explained in section 3.4. In order to estimate the thickness, it is convenient to consider the thickness as a degree of freedom allowing it to set it as an external input. Moreover, slow spatial oscillations due to imperfection during the reconstruction process could introduce a low spatial oscillation on the air-silica interfaces. The following procedure can estimate the loss of drawn fiber begins to take a high-resolution SEM picture of the cross-section of the fiber.

A.1.1 Methods

The picture taken by SEM microscopy despite having a high resolution is composed of a large number of pixels that cannot follow the curvature shape. The main geometrical size of fiber cross-section are: (core diameter= 40μm ; tube radius= 8.36μm;tube thickness= 0.54μm). Two versions of algorithms are proposed: the first one simply converts a raster SEM image of TLF into vector image without any external controls; the second converts an SEM image of TLF into vector image with tube thickness settable as an external parameter. Both of them have as output a DXF CAD file

useful to import in COMSOL environment. Finally, a comparison of them will be done to understand the impact of thickness estimation.

The first algorithm shown in figure A.1 allows converting a cross-section of fiber into boundaries and domains importable in as a CAD file.

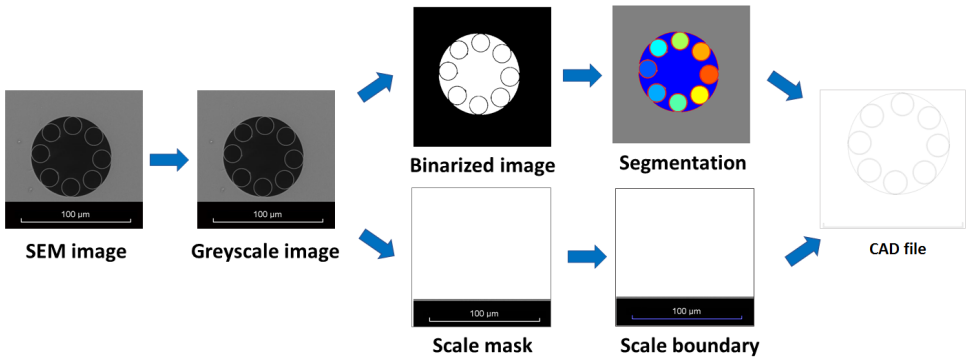

Figure A.1: Algorithm #1 developed to convert a raster image of a TLF into vector image

Initially, the figure is in RGB representation, thus a conversion in gray-scale occurs to have in the same scale representation all the pixel of the image. Then a thresholding image is applied to the picture into the binarized picture. This step has been done to shape a rough structure: it is a crucial step because it separates domains, in other words, it defines roughly pixels belonging to air or silica material. This separation between air and silica is then performed, but it will inherit the features given by the binarization step. Several types of binarization could be done: a fixed threshold is the simplest method, it assigns "0" or "1" if a pixel value is below or above the chosen threshold; otherwise, an adaptive threshold where locally it is assigned a boolean value according to the gradient color of picture [123],[124]. Then a segmentation of the binarized image occurs, it allows to have a set of contours that separates two levels of binarized image [125]. To have the correct proportion of the figure on the imported file an image processing of the scale is needed. Therefore, the scale on the algorithm proposed is processed separately due to different levels of gray leading a thresholding step unreliable. To avoid this, a mask is used to divide the scale from the rest of the image. Finally, segmentation is applied to have the reference line. All boundaries

found are merged with a boundary scale to form a unique CAD file. Unfortunately, the edges detected is not well defined because it follows the path between a pixel. Although the pixel represents the smallest detail of an image, the boundary should have continuous shape avoiding the "staircase effect". Thus Gaussian filtering is applied to smooth the boundaries. The figure A.1 summarizes this procedure in a scheme.

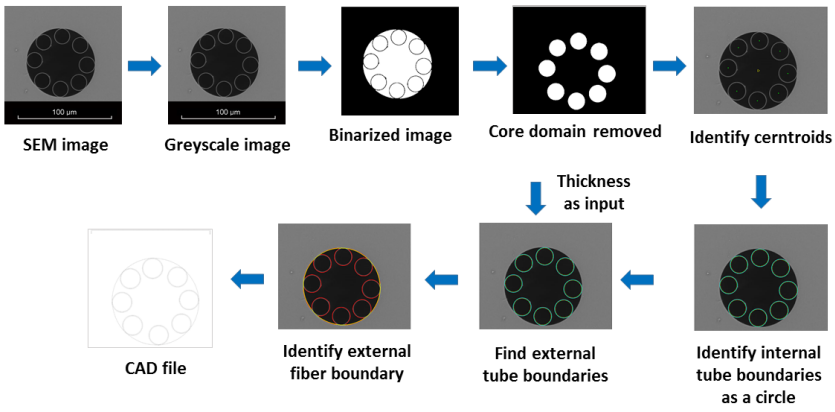

Figure A.2: Algorithm #2 developed to convert a raster image of a TLF into vector image. In algorithm #2 the thickness can be set as input

The second algorithm proposed (figure A.2)is the improvement of the first one. In this case, it was considered as a priority the reconstruction not as an accurate representation of the picture, but as an ideal version of the fiber where the picture is an approximate representation. The second algorithm has in common with the first one until the binarization step. To identify the internal boundaries, the removal of the core is needed. Then, a circular fitting is necessary to convert the internal boundaries into circumferences. As the output of circular fitting is given the radii the centroid points. The reconstruction is performed, the aim is reached: the cross-section is an accurate reconstruction of the SEM picture. Figure A.3 shows the comparison of the simulation results of confinement loss taken by algorithm #1 and #2 with measured loss.

Combining other loss mechanisms as MDL and SSL explained in section 3.6 it is possible to estimate the loss profile.

Then, the model is been applied in another TLF with different geometric size (core

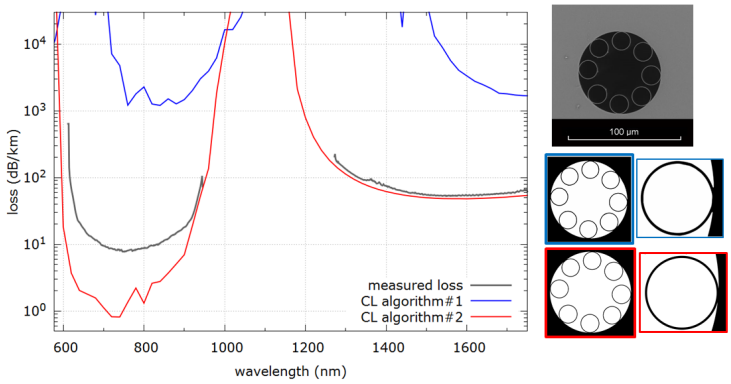

Figure A.3: Comparison of the two algorithms proposed: reconstruction with: algorithm #1 in blue, algorithm #2 in red

diameter= 40μm ; tube radius= 7.83μm;tube thickness= 0.22μm)

According to the results obtained, it is possible to state that the developed model proves effective for estimating loss in hollow-core TLF.

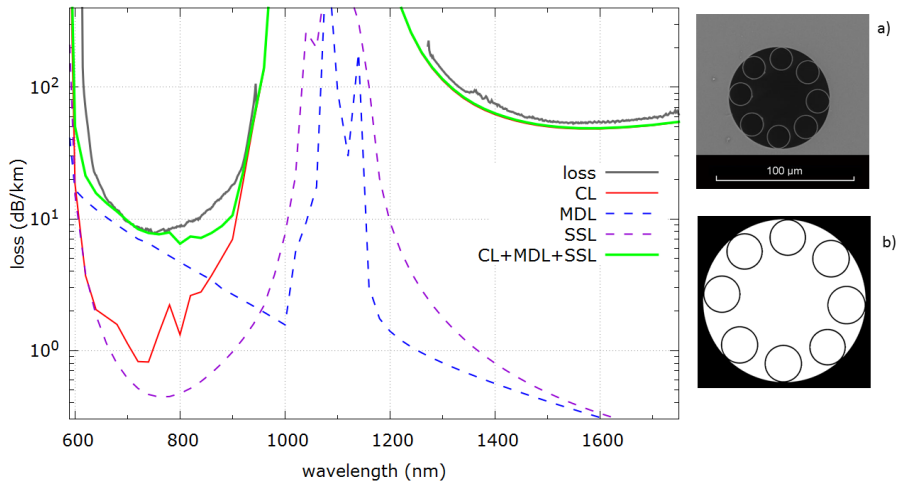

Figure A.4: Fiber reconstruction of cross-section shown in a). In chart are represent the measured loss and the simulated loss: CL, MDL, SSL. The CL is computed by numerical simulation of the reconstructed cross-section b) through the algorithm #2

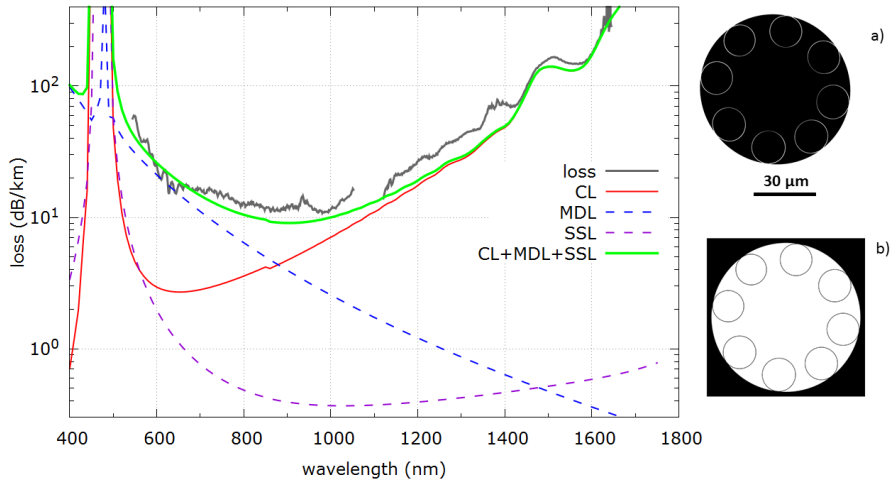

Figure A.5: Fiber reconstruction of cross-section shown in a). The simulated cross-section b)

Appendix B

Publications List

B.1 Journal Articles

1. L. Di Cecilia, S. Cattini, F. Giovanardi, L. Rovati, "Single-arm self-mixing superluminescent diode interferometer for flow measurements," *Journal of Lightwave Technology*, 35(16), 3577-3583 (2017)

2. F. Giovanardi, A. Cucinotta, and Luca Vincetti, "Inhibited coupling guiding hollow fibers for label-free DNA detection," *Opt. Express* 25, 26215-26220 (2017)

3. F. Giovanardi, A. Cucinotta, A. Rozzi, R. Corradini, F. Benabid, L. Rosa, and L. Vincetti, "Hollow Core Inhibited Coupling Fibers for Biological Optical Sensing," *Journal of Lightwave Technology* 37, 2598-2604 (2019)

4. J. Osório, M. Chafer, B. Debord, F. Giovanardi, M. Cordier, M. Maurel, F. Delahaye, F. Amrani, L. Vincetti, F. Gérôme, and F. Benabid, "Tailoring modal properties of inhibited-coupling guiding fibers by cladding modification ". *Scientific Reports* 9, 1376 (2019)

B.2 Conference proceedings

1. F. Giovanardi, C. Molardi ,A. Cucinotta, L. Vincetti , "Hollow-Core Inhibited Coupling Fibers for Label-free DNA Detection", Fotonica 2017, Padua

2. F. Giovanardi, A. Cucinotta, L. Vincetti, "Microstructured Fibers for label-free DNA detection", Fotonica 2018, Lecce

3. J. Osório, M. Chafer, B. Debord, F. Giovanardi, M. Cordier, M. Maurel, F. Delahaye, F. Amrani, L. Vincetti, F. Gérôme, and F. Benabid, "Mode transformation in an inhibited-coupling guiding asymmetric tubular hollow fiber", CLEO 2018: Science and Innovations, SF1K. 6

4. F. Giovanardi, A. Cucinotta, A. Rozzi, R. Corradini, F. Benabid, and L. Vincetti, "Protein detection using hollow-core tube lattice fibers" Optical Sensors, SeM3E. 4, Advanced Photonics Congress, Zurich, 2018

5. F. Giovanardi, A. Cucinotta, A. Rozzi, R. Corradini, F. Benabid, and L. Vincetti, "Experimental demonstration of protein sensing using hollow-core tube lattice fibers", Photonics West Bios 2019, San Francisco

6. F. Giovanardi, A. Cucinotta, L. Vincetti, "Biosensing with Hollow Core Inhibited Coupling Fibers", PIERS 2019, Rome

7. J. H. Osório, M. Chafer, B. Debord, F. Giovanardi, M. Cordier, F. Delahaye, F. Amrani, L. Vincetti, F. Gérôme, and F. Benabid, "Core modal spatial-structuring in inhibited-coupling hollow-core fibers" CLEO/Europe-EQEC, 23-27 June 2019, Munich, Germany

Bibliography

[1] I. Grand View Research, "Biosensors market size, share & trends analysis report by application (agriculture, medical) by technology (thermal, electrochemical, optical), by end use (poc testing, food industry), and segment forecasts, 2019 - 2026," *KBV Research*, 10 2019.

[2] M. A. Cooper, "Optical biosensors in drug discovery," *Nature Reviews Drug Discovery*, vol. 1, no. 7, pp. 515–528, 2002.

[3] A. Hasan, M. Nurunnabi, M. Morshed, A. Paul, A. Polini, T. Kuila, M. Al Hariri, Y.-k. Lee, and A. A. Jaffa, "Recent advances in application of biosensors in tissue engineering," *BioMed research international*, vol. 2014, pp. 307519–307519, 2014. 25165697[pmid].

[4] F. Yu, M. Cann, A. Brunton, W. Wadsworth, and J. Knight, "Single-mode solarization-free hollow-core fiber for ultraviolet pulse delivery," *Opt. Express*, vol. 26, pp. 10879–10887, Apr 2018.

[5] B. Debord, M. Alharbi, A. Benoît, D. Ghosh, M. Dontabactouny, L. Vincetti, J.-M. Blondy, F. Gérôme, and F. Benabid, "Ultra low-loss hypocycloid-core kagome hollow-core photonic crystal fiber for green spectral-range applications," *Opt. Lett.*, vol. 39, pp. 6245–6248, Nov 2014.

[6] S. Eilzer and B. Wedel, "Hollow core optical fibers for industrial ultra short pulse laser beam delivery applications," *Fibers*, vol. 6, no. 4, p. 80, 2018.

[7] X. Wang, D. Ge, W. Ding, Y. Wang, S. Gao, X. Zhang, Y. Sun, J. Li, Z. Chen, and P. Wang, "Hollow-core conjoined-tube fiber for penalty-free data transmission under offset launch conditions," *Optics letters*, vol. 44, no. 9, pp. 2145–2148, 2019.

[8] M. Michieletto, J. K. Lyngsø, C. Jakobsen, J. Lægsgaard, O. Bang, and T. T. Alkeskjold, "Hollow-core fibers for high power pulse delivery," *Optics express*, vol. 24, no. 7, pp. 7103–7119, 2016.

[9] S. Shukla, P. Govender, and A. Tiwari, "Chapter six - polymeric micellar structures for biosensor technology," in *Advances in Biomembranes and Lipid Self-Assembly* (A. Iglic, C. V. Kulkarni, and M. Rappolt, eds.), vol. 24, pp. 143 – 161, Academic Press, 2016.

[10] H. H. Nguyen, S. H. Lee, U. J. Lee, C. D. Fermin, and M. Kim, "Immobilized enzymes in biosensor applications," *Materials (Basel, Switzerland)*, vol. 12, p. 121, Jan 2019. 30609693[pmid].

[11] D. R. Thévenot, K. Toth, R. A. Durst, and G. S. Wilson, "Electrochemical biosensors: recommended definitions and classification1international union of pure and applied chemistry: Physical chemistry division, commission i.7 (biophysical chemistry); analytical chemistry division, commission v.5 (electroanalytical chemistry).1," *Biosensors and Bioelectronics*, vol. 16, no. 1, pp. 121 – 131, 2001.

[12] Y. Zhang, D. Yang, L. Weng, and L. Wang, "Early lung cancer diagnosis by biosensors," *International Journal of Molecular Sciences*, vol. 14, no. 8, pp. 15479–15509, 2013.

[13] T. D. Martins, A. C. C. Ribeiro, H. S. de Camargo, P. A. da Costa Filho, H. P. M. Cavalcante, and D. L. Dias, "New insights on optical biosensors: techniques, construction and application," *State of the Art in Biosensors—General Aspects*, pp. 112–139, 2013.

[14] Y. Chen, R. Ren, H. Pu, X. Guo, J. Chang, G. Zhou, S. Mao, M. Kron, and J. Chen, "Field-effect transistor biosensor for rapid detection of ebola antigen," *Scientific Reports*, vol. 7, no. 1, p. 10974, 2017.

[15] M. Kaisti, "Detection principles of biological and chemical fet sensors," *Biosensors and Bioelectronics*, vol. 98, pp. 437 – 448, 2017.

[16] Y.-C. Syu, W.-E. Hsu, and C.-T. Lin, "Field-effect transistor biosensing: Devices and clinical applications," *ECS Journal of Solid State Science and Technology*, vol. 7, no. 7, pp. Q3196–Q3207, 2018.

[17] M. Pohanka, "Overview of piezoelectric biosensors, immunosensors and dna sensors and their applications," *Materials (Basel, Switzerland)*, vol. 11, p. 448, Mar 2018.

[18] S. Tombelli, "2 - piezoelectric biosensors for medical applications," in *Biosensors for Medical Applications* (S. Higson, ed.), Woodhead Publishing Series in Biomaterials, pp. 41 – 64, Woodhead Publishing, 2012.

[19] A. Socorro-Leránoz, D. Santano, I. D. Villar, and I. Matias, "Trends in the design of wavelength-based optical fibre biosensors (2008-2018)," *Biosensors and Bioelectronics: X*, vol. 1, p. 100015, 2019.

[20] A. Wang, H. Xiao, J. Wang, Z. Wang, W. Zhao, and R. G. May, "Self-calibrated interferometric-intensity-based optical fiber sensors," *J. Lightwave Technol.*, vol. 19, p. 1495, Oct 2001.

[21] Z. Gharsallah, M. Najjar, B. Suthar, and V. Janyani, "High sensitivity and ultra-compact optical biosensor for detection of urea concentration," *Optical and Quantum Electronics*, vol. 50, no. 6, p. 249, 2018.

[22] H. Shafiee, E. A. Lidstone, M. Jahangir, F. Inci, E. Hanhauser, T. J. Henrich, D. R. Kuritzkes, B. T. Cunningham, and U. Demirci, "Nanostructured optical photonic crystal biosensor for hiv viral load measurement," *Scientific Reports*, vol. 4, no. 1, p. 4116, 2014.

[23] W. Pongruengkiat and S. Pechprasarn, "Whispering-gallery mode resonators for detecting cancer," *Sensors*, vol. 17, no. 9, 2017.

[24] A. Tavousi, M. Rakhshani, and M. Mansouri-Birjandi, "High sensitivity label-free refractometer based biosensor applicable to glycated hemoglobin detection in human blood using all-circular photonic crystal ring resonators," *Optics Communications*, vol. 429, pp. 166 – 174, 2018.

[25] N. Peserico, A. Annoni, A. Varriale, S. D'Auria, L. Bellieres, F. Cuesta-Soto, M. Rodrigo, S. Peransi, and A. Melloni, "Experimental demonstration of integrated photonic free-label biosensor for cbrn threats using micro-ring resonators," in *2016 18th International Conference on Transparent Optical Networks (ICTON)*, pp. 1–4, IEEE, 2016.

[26] A. Nabok, A. Al-Rubaye, A. Al-Jawdah, A. Tsargorodska, J.-L. Marty, G. Catanante, A. Szekacs, and E. Takacs, "Novel optical biosensing technologies for detection of mycotoxins," *Optics & Laser Technology*, vol. 109, pp. 212 – 221, 2019.

[27] M. R. N. Monton, E. M. Forsberg, and J. D. Brennan, "Tailoring sol gel-derived silica materials for optical biosensing," *Chemistry of Materials*, vol. 24, no. 5, pp. 796–811, 2012.

[28] N. Jiang, R. Ahmed, A. A. Rifat, J. Guo, Y. Yin, Y. Montelongo, H. Butt, and A. K. Yetisen, "Functionalized flexible soft polymer optical fibers for laser photomedicine," *Advanced Optical Materials*, vol. 6, no. 3, p. 1701118, 2018.

[29] A. Rosenthal, S. Kellnberger, D. Bozhko, A. Chekkoury, M. Omar, D. Razansky, and V. Ntziachristos, "Sensitive interferometric detection of ultrasound for minimally invasive clinical imaging applications," *Laser & Photonics Reviews*, vol. 8, no. 3, pp. 450–457, 2014.

[30] B. Carotenuto, A. Ricciardi, A. Micco, E. Amorizzo, M. Mercieri, A. Cutolo, and A. Cusano, "Smart optical catheters for epidurals," *Sensors*, vol. 18, no. 7, 2018.

[31] G. Cheymol, B. Brichard, and J. F. Villard, "Fiber optics for metrology in nuclear research reactors applications to dimensional measurements," *IEEE Transactions on Nuclear Science*, vol. 58, pp. 1895–1902, Aug 2011.

[32] W. Hou, G. Liu, and M. Han, "A novel, high-resolution, high-speed fiber-optic temperature sensor for oceanographic applications," in *2015 IEEE/OES Eleveth Current, Waves and Turbulence Measurement (CWTM)*, pp. 1–4, March 2015.

[33] M. Lismont, N. Vandewalle, B. Joris, and L. Dreesen, "Fiber based optofluidic biosensors," *Applied Physics Letters*, vol. 105, no. 13, p. 133701, 2014.

[34] Z. Liu, Y. Wei, Y. Zhang, Y. Wang, E. Zhao, Y. Zhang, J. Yang, C. Liu, and L. Yuan, "A multi-channel fiber spr sensor based on tdm technology," *Sensors and Actuators B: Chemical*, vol. 226, pp. 326 – 331, 2016.

[35] A. Leung, P. M. Shankar, and R. Mutharasan, "A review of fiber-optic biosensors," *Sensors and Actuators B: Chemical*, vol. 125, no. 2, pp. 688 – 703, 2007.

[36] P. Vaiano, B. Carotenuto, M. Pisco, A. Ricciardi, G. Quero, M. Consales, A. Crescitelli, E. Esposito, and A. Cusano, "Lab on fiber technology for biological sensing applications," *Laser & Photonics Reviews*, vol. 10, no. 6, pp. 922–961, 2016.

[37] M. Principe, M. Consales, A. Micco, A. Crescitelli, G. Castaldi, E. Esposito, V. La Ferrara, A. Cutolo, V. Galdi, and A. Cusano, "Optical fiber meta-tips," *Light: Science & Applications*, vol. 6, no. 3, pp. e16226–e16226, 2017.

[38] C. A. J. Gouveia, J. M. Baptista, and P. A. Jorge, "Refractometric optical fiber platforms for label free sensing," in *Current Developments in Optical Fiber Technology* (S. W. Harun and H. Arof, eds.), ch. 13, Rijeka: IntechOpen, 2013.

[39] A. Leung, P. Mohana Shankar, and R. Mutharasan, "Evanescent field tapered fiber optic biosensors (tfobs): Fabrication, antibody immobilization and detection," *Nova: New York NY, USA*, 2012.

[40] K. Sapsford, C. R. Taitt, and F. S. Ligler, "Chapter 3 - planar waveguides for fluorescence biosensors," in *Optical Biosensors (Second Edition)* (F. S. Ligler and C. R. Taitt, eds.), pp. 139 – 184, Amsterdam: Elsevier, second edition ed., 2008.

[41] Y. Tian, W. Wang, N. Wu, X. Zou, and X. Wang, "Tapered optical fiber sensor for label-free detection of biomolecules," *Sensors*, vol. 11, no. 4, pp. 3780–3790, 2011.

[42] N. H. Zainuddin, H. Y. Chee, M. Z. Ahmad, M. A. Mahdi, M. H. Abu Bakar, and M. H. Yaacob, "Sensitive leptospira dna detection using tapered optical fiber sensor," *Journal of Biophotonics*, vol. 11, no. 8, p. e201700363, 2018.

[43] P. Wang, L. Bo, Y. Semenova, G. Farrell, and G. Brambilla, "Optical microfibre based photonic components and their applications in label-free biosensing," *Biosensors*, vol. 5, no. 3, pp. 471–499, 2015.

[44] S. J. Zalyubovskiy, M. Bogdanova, A. Deinega, Y. Lozovik, A. D. Pris, K. H. An, W. P. Hall, and R. A. Potyrailo, "Theoretical limit of localized surface plasmon resonance sensitivity to local refractive index change and its comparison to conventional surface plasmon resonance sensor," *J. Opt. Soc. Am. A*, vol. 29, pp. 994–1002, Jun 2012.

[45] C. Francesco, B. Francesco, T. Sara, T. Cosimo, and G. Ambra, "Biosensing with optical fiber gratings," *nanophotonics*, vol. 6, p. 663, 2019 2017. 4.

[46] M. Barozzi, A. Manicardi, A. Vannucci, A. Candiani, M. Sozzi, M. Konstantaki, S. Pissadakis, R. Corradini, S. Selleri, and A. Cucinotta, "Optical Fiber Sensors for Label-Free DNA Detection," *J. Lightw. Technol.*, vol. 35, pp. 3461–3472, Aug. 2017.

[47] A. Candiani, A. Bertucci, S. Giannetti, M. Konstantaki, A. Manicardi, S. Pissadakis, A. Cucinotta, R. Corradini, and S. Selleri, "Label-free dna biosensor based on a peptide nucleic acid-functionalized microstructured optical fiber-bragg grating," *J. Biomed. Opt.*, vol. 18, p. 18, 2013.

[48] A. Bertucci, A. Manicardi, A. Candiani, S. Giannetti, A. Cucinotta, G. Spoto, M. Konstantaki, S. Pissadakis, S. Selleri, and R. Corradini, "Detection of unamplified genomic dna by a pna-based microstructured optical fiber (mof) bragg-grating optofluidic system," *Biosens. Bioelectron.*, vol. 63, pp. 248 – 254, 2015.

[49] C. Boudoux, *Fundamentals of Biomedical Optics: From Light Interaction with Atoms and Molecules to Complex Imaging Systems*. Pollux, 2016.

[50] N. Kuruba and T. Lu, "Hollow fiber coupler sensor," *Sensors*, vol. 19, no. 4, 2019.

[51] J. Homola, S. S. Yee, and G. Gauglitz, "Surface plasmon resonance sensors," *Sensors and Actuators B: Chemical*, vol. 54, no. 1-2, pp. 3–15, 1999.

[52] B. Liedberg, C. Nylander, and I. Lundström, "Biosensing with surface plasmon resonance—how it all started," *Biosensors and Bioelectronics*, vol. 10, no. 8, pp. i–ix, 1995.

[53] P. Zubiate, C. R. Zamarreno, I. Del Villar, I. R. Matias, and F. J. Arregui, "Experimental study and sensing applications of polarization-dependent lossy

mode resonances generated by d-shape coated optical fibers," *Journal of Lightwave Technology*, vol. 33, no. 12, pp. 2412–2418, 2015.

[54] B.-H. Liu, Y.-X. Jiang, X.-S. Zhu, X.-L. Tang, and Y.-W. Shi, "Hollow fiber surface plasmon resonance sensor for the detection of liquid with high refractive index," *Opt. Express*, vol. 21, pp. 32349–32357, Dec 2013.

[55] D. U. S., C. Y. Fu, K. S. Soh, B. Ramaswamy, A. Kumar, and M. Olivo, "Highly sensitive sers detection of cancer proteins in low sample volume using hollow core photonic crystal fiber," *Biosensors and Bioelectronics*, vol. 33, no. 1, pp. 293 – 298, 2012.

[56] E. J. Smythe, M. D. Dickey, E. Schonbrun, K. B. Crozier, G. M. Whitesides, and F. Capasso, "Functionalized fiber optic devices for surface enhanced raman scattering detection and optical trapping," in *2009 Conference on Lasers and Electro-Optics and 2009 Conference on Quantum electronics and Laser Science Conference*, pp. 1–2, June 2009.

[57] G. F. Andrade, M. Fan, and A. G. Brolo, "Multilayer silver nanoparticles-modified optical fiber tip for high performance sers remote sensing," *Biosensors and Bioelectronics*, vol. 25, no. 10, pp. 2270 – 2275, 2010.

[58] H. Yan, C. Gu, C. Yang, J. Liu, G. Jin, J. Zhang, L. Hou, and Y. Yao, "Hollow core photonic crystal fiber surface-enhanced raman probe," *Applied Physics Letters*, vol. 89, no. 20, p. 204101, 2006.

[59] A. Khetani, A. Momenpour, E. I. Alarcon, and H. Anis, "Hollow core photonic crystal fiber for monitoring leukemia cells using surface enhanced raman scattering (sers)," *Biomed. Opt. Express*, vol. 6, pp. 4599–4609, Nov 2015.

[60] S. Li, L. Xia, W. Li, X. Chen, Z. Yang, and J. Xia, "All-fiber sers sensing with a depressed double cladding fiber probe embedded in a microfluidic chip," *Appl. Opt.*, vol. 58, pp. 7929–7934, Oct 2019.

[61] L. C. Shriver-Lake, K. A. Breslin, P. T. Charles, D. W. Conrad, J. P. Golden, and F. S. Ligler, "Detection of tnt in water using an evanescent wave fiber-optic biosensor," *Analytical Chemistry*, vol. 67, no. 14, pp. 2431–2435, 1995.

[62] X. Liu and W. Tan, "A fiber-optic evanescent wave dna biosensor based on novel molecular beacons," *Analytical Chemistry*, vol. 71, no. 22, pp. 5054–5059, 1999. PMID: 10575961.

[63] J. Sun, C.-C. Chan, Y. Zhang, and P. Shum, "Analysis of hollow-core photonic bandgap fibers for evanescent wave biosensing," *Journal of Biomedical Optics*, vol. 13, no. 5, pp. 1 – 6, 2008.

[64] A. Bekmurzayeva, K. Dukenbayev, M. Shaimerdenova, I. Bekniyazov, T. Ayupova, M. Sypabekova, C. Molardi, and D. Tosi, "Etched fiber bragg grating biosensor functionalized with aptamers for detection of thrombin," *Sensors*, vol. 18, no. 12, 2018.

[65] Jin-Fei Ding, A. P. Zhang, Li-Yang Shao, Jin-Hua Yan, and Sailing He, "Fiber-taper seeded long-period grating pair as a highly sensitive refractive-index sensor," *IEEE Photonics Technology Letters*, vol. 17, pp. 1247–1249, June 2005.

[66] J. Ma, Y. Zhou, X. Bai, K. Chen, and B.-O. Guan, "High-sensitivity and fast-response fiber-tip fabry–pérot hydrogen sensor with suspended palladium-decorated graphene," *Nanoscale*, vol. 11, pp. 15821–15827, 2019.

[67] Y. Zhang, X. Chen, Y. Wang, K. L. Cooper, and A. Wang, "Microgap multicavity fabry–pérot biosensor," *Journal of Lightwave Technology*, vol. 25, pp. 1797–1804, July 2007.

[68] X. Li, L. V. Nguyen, Y. Zhao, H. Ebendorff-Heidepriem, and S. C. Warren-Smith, "High-sensitivity sagnac-interferometer biosensor based on exposed core microstructured optical fiber," *Sensors and Actuators B: Chemical*, vol. 269, pp. 103 – 109, 2018.

[69] B. Sciacca and T. M. Monro, "Dip biosensor based on localized surface plasmon resonance at the tip of an optical fiber," *Langmuir*, vol. 30, no. 3, pp. 946–954, 2014. PMID: 24397817.

[70] J. H. Ahn, T. Y. Seong, W. M. Kim, T. S. Lee, I. Kim, and K.-S. Lee, "Fiber-optic waveguide coupled surface plasmon resonance sensor," *Opt. Express*, vol. 20, pp. 21729–21738, Sep 2012.

[71] L. Zhao, H. Han, N. Luan, J. Liu, L. Song, and Y. Hu, "A temperature plasmonic sensor based on a side opening hollow fiber filled with high refractive index sensing medium," *Sensors*, vol. 19, no. 17, 2019.

[72] Y. Zhang, C. Gu, A. M. Schwartzberg, and J. Z. Zhang, "Surface-enhanced raman scattering sensor based on d-shaped fiber," *Applied Physics Letters*, vol. 87, no. 12, p. 123105, 2005.

[73] Y. Geng, Y. Xu, X. Tan, L. Wang, X. Li, Y. Du, and X. Hong, "A simplified hollow-core photonic crystal fiber sers probe with a fully filled photoreduction silver nanoprism," *Sensors*, vol. 18, no. 6, 2018.

[74] J. K. Pavel Damborský, Juraj Vitel, "Optical biosensors," *Essays Biochemistry*, vol. 60, no. June, pp. 91–100, 2016.

[75] S. Mehrabani, A. J. Maker, and A. M. Armani, "Hybrid integrated label-free chemical and biological sensors," *Sensors*, vol. 14, no. 4, pp. 5890–5928, 2014.

[76] T. A. Birks, P. J. Roberts, P. S. J. Russell, D. M. Atkin, and T. J. Shepherd, "Full 2-d photonic bandgaps in silica/air structures," *Electronics Letters*, vol. 31, pp. 1941–1943, Oct 1995.

[77] P. S. J. Russell, "Optics of floquet-bloch waves in dielectric gratings," *Applied Physics B*, vol. 39, no. 4, pp. 231–246, 1986.

[78] F. H. M. Faisal and J. Z. Kamiński, "Floquet-bloch theory of high-harmonic generation in periodic structures," *Phys. Rev. A*, vol. 56, pp. 748–762, Jul 1997.

[79] F. Benabid and P. Roberts, "Linear and nonlinear optical properties of hollow core photonic crystal fiber," *Journal of Modern Optics*, vol. 58, no. 2, pp. 87–124, 2011.

[80] P. S. Light, F. Couny, Y. ying Wang, N. V. Wheeler, P. J. Roberts, and F. Benabid, "Double photonic bandgap hollow-core photonic crystal fiber.," *Optics express*, vol. 17 18, pp. 16238–43, 2009.

[81] B. Debord, A. Amsanpally, M. Chafer, A. Baz, M. Maurel, J. M. Blondy, E. Hugonnot, F. Scol, L. Vincetti, F. Gérôme, and F. Benabid, "Ultralow transmission loss in inhibited-coupling guiding hollow fibers," *Optica*, vol. 4, pp. 209–217, Feb. 2017.

[82] L. Vincetti and V. Setti, "Waveguiding mechanism in tube lattice fibers," *Opt. Express*, vol. 18, pp. 23133–23146, Oct. 2010.

[83] C. Wei, R. J. Weiblen, C. R. Menyuk, and J. Hu, "Negative curvature fibers," *Adv. Opt. Photon.*, vol. 9, pp. 504–561, Sep 2017.

[84] F. Poletti, "Nested antiresonant nodeless hollow core fiber," *Opt. Express*, vol. 22, pp. 23807–23828, Oct 2014.

[85] T. D. Bradley, J. R. Hayes, Y. Chen, G. T. Jasion, S. R. Sandoghchi, R. Slavik, E. N. Fokoua, S. Bawn, H. Sakr, I. A. Davidson, A. Taranta, J. P. Thomas, M. N. Petrovich, D. J. Richardson, and F. Poletti, "Record low-loss 1.3db/km data transmitting antiresonant hollow core fibre," in *2018 European Conference on Optical Communication (ECOC)*, pp. 1–3, Sep. 2018.

[86] B. Debord, F. Amrani, L. Vincetti, F. Gérôme, and F. Benabid, "Hollow-core fiber technology: The rising of gas photonics," *Fibers*, vol. 7, no. 2, 2019.

[87] F. Couny, F. Benabid, and P. S. Light, "Large-pitch kagome-structured hollow-core photonic crystal fiber," *Opt. Lett.*, vol. 31, pp. 3574–3576, Dec 2006.

[88] F. Benabid, J. C. Knight, G. Antonopoulos, and P. S. J. Russell, "Stimulated raman scattering in hydrogen-filled hollow-core photonic crystal fiber," *Science*, vol. 298, no. 5592, pp. 399–402, 2002.

[89] S.-f. Gao, Y.-y. Wang, W. Ding, D.-l. Jiang, S. Gu, X. Zhang, and P. Wang, "Hollow-core conjoined-tube negative-curvature fibre with ultralow loss," *Nature Communications*, vol. 9, no. 1, p. 2828, 2018.

[90] E. A. J. Marcatili and R. A. Schmeltzer, "Hollow metallic and dielectric waveguides for long distance optical transmission and lasers," *Bell System Technical Journal*, vol. 43, no. 4, pp. 1783–1809, 1964.

[91] L. Vincetti and L. Rosa, "A simple analytical model for confinement loss estimation in hollow-core tube lattice fibers," *Opt. Express*, vol. 27, pp. 5230–5237, Feb 2019.

[92] M. M. Z. Kharadly and J. E. Lewis, "Properties of dielectric-tube waveguides," *Proc. IEE*, vol. 116, pp. 214–224, Feb. 1969.

[93] A. K. Mudraboyina and J. Sabarinathan, "Protein Binding Detection Using On-Chip Silicon Gratings," *Sensors*, vol. 11, pp. 11295–11304, Nov. 2011.

[94] A. Candiani, M. Sozzi, A. Cucinotta, S. Selleri, R. Veneziano, R. Corradini, R. Marchelli, P. Childs, and S. Pissadakis, "Optical fiber ring cavity sensor for label-free dna detection," *IEEE J. Sel. Top. Quantum Electron.*, vol. 18, pp. 1176–1183, May 2012.

[95] P. Uebel, M. C. Günendi, M. H. Frosz, G. Ahmed, N. N. Edavalath, J.-M. Ménard, and P. S. Russell, "Broadband robustly single-mode hollow-core pcf by resonant filtering of higher-order modes," *Opt. Lett.*, vol. 41, pp. 1961–1964, May 2016.

[96] A. N. Kolyadin, A. F. Kosolapov, A. D. Pryamikov, A. S. Biriukov, V. G. Plotnichenko, and E. M. Dianov, "Light transmission in negative curvature hollow core fiber in extremely high material loss region," *Opt. Express*, vol. 21, pp. 9514–9519, Apr 2013.

[97] S. fei Gao, Y. ying Wang, X. lu Liu, C. Hong, S. Gu, and P. Wang, "Nodeless hollow-core fiber for the visible spectral range," *Opt. Lett.*, vol. 42, pp. 61–64, Jan 2017.

[98] N. V. Wheeler, A. M. Heidt, N. K. Baddela, E. N. Fokoua, J. R. Hayes, S. R. Sandoghchi, F. Poletti, M. N. Petrovich, and D. J. Richardson, "Low-loss and low-bend-sensitivity mid-infrared guidance in a hollow-core–photonic-bandgap fiber," *Opt. Lett.*, vol. 39, pp. 295–298, Jan 2014.

[99] P. J. Roberts, F. Couny, H. Sabert, B. J. Mangan, D. P. Williams, L. Farr, M. W. Mason, A. Tomlinson, T. A. Birks, J. C. Knight, and P. S. Russell, "Ultimate low loss of hollow-core photonic crystal fibres," *Opt. Express*, vol. 13, pp. 236–244, Jan 2005.

[100] E. N. Fokoua, F. Poletti, and D. J. Richardson, "Analysis of light scattering from surface roughness in hollow-core photonic bandgap fibers," *Opt. Express*, vol. 20, pp. 20980–20991, Sep 2012.

[101] K. Petermann, "Theory of microbending loss in monomode fibres with arbitrary refractive index profile," *Archiv Elektronik und Uebertragungstechnik*, vol. 30, pp. 337–342, Sep 1976.

[102] H. Taylor, "Bending effects in optical fibers," *Journal of Lightwave Technology*, vol. 2, pp. 617–628, October 1984.

[103] W. Belardi and J. C. Knight, "Hollow antiresonant fibers with low bending loss," *Opt. Express*, vol. 22, pp. 10091–10096, Apr 2014.

[104] F. Giovanardi, A. Cucinotta, and L. Vincetti, "Inhibited coupling guiding hollow fibers for label-free DNA detection," *Opt. Express*, vol. 25, pp. 26215–26220, Oct. 2017.

[105] P. Weber, D. Ohlendorf, J. Wendoloski, and F. Salemme, "Structural origins of high-affinity biotin binding to streptavidin," *Science*, vol. 243, no. 4887, pp. 85–88, 1989.

[106] R. A. Vijayendran and D. E. Leckband, "A quantitative assessment of heterogeneity for surface-immobilized proteins," *Analytical Chemistry*, vol. 73, pp. 471–480, Feb 2001.

[107] Y. Guo, J. Y. Ye, C. Divin, B. Huang, T. P. Thomas, J. R. J. Baker, and T. B. Norris, "Real-time biomolecular binding detection using a sensitive photonic crystal biosensor," *Analytical chemistry*, vol. 82, pp. 5211–5218, Jun 2010. 20486666[pmid].

[108] S. Sivasankar, S. Subramaniam, and D. Leckband, "Direct molecular level measurements of the electrostatic properties of a protein surface," *Proceedings of the National Academy of Sciences*, vol. 95, no. 22, pp. 12961–12966, 1998.

[109] N. A. Lapin and Y. J. Chabal, "Infrared characterization of biotinylated silicon oxide surfaces, surface stability, and specific attachment of streptavidin," *The journal of physical chemistry. B*, vol. 113, pp. 8776–8783, Jun 2009. 19489542[pmid].

[110] A. V. Kabashin, P. Evans, S. Pastkovsky, W. Hendren, G. A. Wurtz, R. Atkinson, R. Pollard, V. A. Podolskiy, and A. V. Zayats, "Plasmonic nanorod metamaterials for biosensing," *Nature Materials*, vol. 8, no. 11, pp. 867–871, 2009.

[111] R. Raiteri, M. Grattarola, H.-J. Butt, and P. Skládal, "Micromechanical cantilever-based biosensors," *Sensors and Actuators B: Chemical*, vol. 79, no. 2, pp. 115 – 126, 2001.

[112] T. Kawato, E. Mizohata, T. Meshizuka, H. Doi, T. Kawamura, H. Matsumura, K. Yumura, K. Tsumoto, T. Kodama, T. Inoue, and A. Sugiyama, "Crystal structure of streptavidin mutant with low immunogenicity," *Journal of Bioscience and Bioengineering*, vol. 119, no. 6, pp. 642 – 647, 2015.

[113] X. Chu and J. Wang, "Specificity and affinity quantification of flexible recognition from underlying energy landscape topography," *PLoS computational biology*, vol. 10, pp. e1003782–e1003782, Aug 2014. 25144525[pmid].

[114] J. H. Osório, M. Chafer, B. Debord, F. Giovanardi, M. Cordier, M. Maurel, F. Delahaye, F. Amrani, L. Vincetti, F. Gérôme, and F. Benabid, "Tailoring modal properties of inhibited-coupling guiding fibers by cladding modification," *Scientific Reports*, vol. 9, no. 1, p. 1376, 2019.

[115] F. Yu, W. J. Wadsworth, and J. C. Knight, "Low loss silica hollow core fibers for 3–4 μm spectral region," *Opt. Express*, vol. 20, pp. 11153–11158, May 2012.

[116] A. Hartung, J. Kobelke, A. Schwuchow, K. Wondraczek, J. Bierlich, J. Popp, T. Frosch, and M. A. Schmidt, "Double antiresonant hollow core fiber – guidance in the deep ultraviolet by modified tunneling leaky modes," *Opt. Express*, vol. 22, pp. 19131–19140, Aug 2014.

[117] S.-f. Gao, Y.-y. Wang, W. Ding, Y.-f. Hong, and P. Wang, "Conquering the rayleigh scattering limit of silica glass fiber at visible wavelengths with a hollow-core fiber approach," *Laser & Photonics Reviews*, vol. n/a, no. n/a, p. 1900241, 2019.

[118] T. Balciunas, C. Fourcade-Dutin, G. Fan, T. Witting, A. A. Voronin, A. M. Zheltikov, F. Gerome, G. G. Paulus, A. Baltuska, and F. Benabid, "A strong-field driver in the single-cycle regime based on self-compression in a kagome fibre," *Nature Communications*, vol. 6, 2015.

[119] M. Maurel, M. Chafer, A. Amsanpally, M. Adnan, F. Amrani, B. Debord, L. Vincetti, F. Gérôme, and F. Benabid, "Optimized inhibited-coupling kagome fibers at yb-nd:yag (8.5 db/km) and ti:sa (30 db/km) ranges," *Opt. Lett.*, vol. 43, pp. 1598–1601, Apr 2018.

[120] T. A. Birks, P. J. Roberts, P. S. J. Russell, D. M. Atkin, and T. J. Shepherd, "Full 2-d photonic bandgaps in silica/air structures," *Electronics Letters*, vol. 31, pp. 1941–1943, Oct 1995.

[121] J. C. Knight, T. A. Birks, P. S. J. Russell, and D. M. Atkin, "All-silica single-mode optical fiber with photonic crystal cladding," *Opt. Lett.*, vol. 21, pp. 1547–1549, Oct 1996.

[122] E. N. Fokoua, S. R. Sandoghchi, Y. Chen, G. T. Jasion, N. V. Wheeler, N. K. Baddela, J. R. Hayes, M. N. Petrovich, D. J. Richardson, and F. Poletti, "Accurate modelling of fabricated hollow-core photonic bandgap fibers," *Opt. Express*, vol. 23, pp. 23117–23132, Sep 2015.

[123] F. H. Chan, F. K. Lam, and H. Zhu, "Adaptive thresholding by variational method," *IEEE Transactions on Image Processing*, vol. 7, no. 3, pp. 468–473, 1998.

[124] J. M. McHugh, J. Konrad, V. Saligrama, and P.-M. Jodoin, "Foreground-adaptive background subtraction," *IEEE Signal Processing Letters*, vol. 16, no. 5, pp. 390–393, 2009.

[125] J. C. Russ, *The image processing handbook*. CRC press, 2016.